

Luminescence dating reveals late Quaternary evolution of the Pearl River Delta estuary (China) in response to global climate and sea-level changes

Lei Gao ^{a,b}, Hao Long ^{a,b,c,*}, Jingran Zhang ^d, Xiaoling Huang ^{a,d}, Zhigang Zhang ^d, Aimin Zhang ^a, Leilei Yuan ^e, Xiaohua Zhou ^f, Ren Jiang ^f

^a State Key Laboratory of Lake and Watershed Science for Water Security, Nanjing Institute of Geography and Limnology, Chinese Academy of Sciences, Nanjing 211135, China

^b State Key Laboratory of Lake Science and Environment, Nanjing Institute of Geography and Limnology, Chinese Academy of Sciences, Nanjing, 210008, China

^c University of Chinese Academy of Sciences, Nanjing, 211135, China

^d School of Geography, Nanjing Normal University, Jiangsu Centre for Collaborative Innovation in Geographical Information Resource Development and Application, Key Laboratory of Virtual Geographic Environment, Ministry of Education of China, Nanjing, 210023, China

^e Geotechnical Survey Design Institute, Shanghai Urban Construction Design and Research Institute (Group) Co., Ltd., Shanghai, 200125, China

^f Nanjing Center, China Geological Survey, Nanjing, 210016, China

ARTICLE INFO

Handling Editor: Biagio Giaccio

Keywords:

Pearl River Delta
Sedimentary sequence
Luminescence dating
Depositional history
Global climate and sea level change

ABSTRACT

The dynamic interaction at the interface between the alluvial river networks of the Pearl River Delta (PRD) plain and the northern continental shelf of the South China Sea has spurred the development of world-class port clusters, advanced manufacturing belts, and innovation-led urban agglomerations. Investigating the sedimentary evolution of large river deltas holds crucial significance for deciphering regional geological processes, paleo-environmental changes, sea-level fluctuations, and human-natural interactions, offering insights into coastal system resilience and sustainable management in the context of global climate change. However, the chronological framework of the late Quaternary depositional stratigraphy in this region and the formation timing of the initial marine transgression events have not yet been conclusively established. Here, we reconstruct the late Quaternary sedimentary history of the present PRD estuary based on sedimentological investigations and multi-method dating of a 53-m-long drill core (CP-QZ04). Sedimentological analyses encompass lithological features, photographic documentation, and grain size variations of core sediments. The chronology of this study borehole was established by combining quartz optically stimulated luminescence (OSL) dating, polymineral grains (4–11 µm) and single-grain/multi-grain K-feldspar post-infrared infrared (pIRIR₂₂₅) dating, and radiocarbon (¹⁴C) ages. Collectively, we established the first reliable chronology covering approximately 311 ka for the PRD stratigraphy in its present estuary region, which has never been reported in previous studies. Stratigraphic analysis indicates that the Late Quaternary depositional sequence within the present PRD estuary records distinct paleoenvironmental stages. Pre-Marine Isotope Stage (MIS) 9 deposition was dominated by alluvial conglomerates that underwent intense weathering. This was succeeded by a fluvial-dominated terrestrial depositional regime that persisted from MIS 9 to MIS 7 (ca. 311–196 ka). During the MIS 6/5 transition (196–132 ka), the sedimentary facies shifted to coastal plain deposits, reflecting alternation of marine regression and transgression associated with sea-level fluctuations. The Holocene sequence (<11.7 ka) exhibits a characteristic vertical succession from intertidal mudflat to prodelta facies, indicating progressive marine inundation. Notably, this study identifies two major depositional hiatuses within the sequence: the first corresponding to MIS 5 (130–71 ka) and the second spanning MIS 4 to MIS 2, extending into early Holocene (71–9 ka). These stratigraphic discontinuities, marked by abrupt lithological contacts and paleosol development, likely reflect eustatic sea-level fluctuations, subaerial exposure, surface erosion and/or depocenter migration. In contrast, those terrestrial-marine interactions in this core are primarily governed by glacial-interglacial cycles, characterized by enhanced terrestrial input during warm interglacial periods and intensified marine influence during sea-level highstands, although modulated by local sediment flux and tectonic settings. Regional correlations align the late Quaternary depositional patterns of the present PRD estuary with those of its inland plain and adjacent coastal records in southern China,

* Corresponding author. State Key Laboratory of Lake and Watershed Science for Water Security, Nanjing Institute of Geography and Limnology, Chinese Academy of Sciences, Nanjing 211135, China.

E-mail address: longhao@niglas.ac.cn (H. Long).

highlighting the dominant control of global climatic and eustatic factors on coastal evolutionary processes. This study establishes a robust framework for understanding delta-estuary system responses to late Quaternary environmental changes, thereby projecting future coastal dynamics under climate-driven sea-level rise scenarios.

1. Introduction

Coastal river deltas, which sustain human populations globally while providing critical ecosystem services (Anthony et al., 2024; Chan et al., 2024), exhibit significant vulnerability to both long-term geological-scale climate shifts and anthropogenic pressures since the proposed onset of the Anthropocene (Bianchi and Allison, 2009; Nienhuis et al., 2020; Zhu et al., 2024). As a major delta in Asia, the Pearl River Delta has historically given rise to several mega-cites, such as Guangzhou, Shenzhen, Hong Kong, and Macau, along with numerous urban centers in southern China. Situated with the transition zone between the fluvial-dominated delta of the Pearl River and the marine environments of the South China Sea's (SCS) northern shelf, this deltaic system has fostered extensive economic development (Lancia et al., 2020). Currently, a world-class bay area and globally leading urban cluster have emerged around the Pearl River estuary, officially designated as the "Guangdong-Hong Kong-Macao Greater Bay Area" (Secretariat of Greater Bay Area Science, 2024). Understanding the formation mechanisms and evolutionary pathways of the Pearl River Delta across geological timescales is essential for balancing its natural trajectory with human-driven urbanization and industrialization. Maintaining such equilibrium preserves the delta's ecological resilience and resource sustainability, securing its long-term socio-ecological functionality (Anthony et al., 2024; Chan et al., 2024).

The Pearl River Delta's depositional history is governed by interactions among tectonic activity, climate change, sea-level fluctuations, hydrodynamic conditions, and sediment supplies, as well as weathering and erosion processes. These factors collectively define the delta's environmental and geological evolution (Strong et al., 2013; Yu et al., 2016, 2023; Zong et al., 2016; Xiong et al., 2018b; Sheng et al., 2024). Despite substantial research advances in recent decades (Zong et al., 2009a, 2012; Tang et al., 2010, 2011; He et al., 2017; Xiong et al., 2018b, 2020; Chen et al., 2019, 2023; Fu et al., 2020a; Sheng et al., 2024), establishing a unified framework of its late Quaternary sedimentary history remains challenging. This stems primarily from limited reliable chronological control on pre-Holocene sediments and stratigraphy. For instance, previous studies have reconstructed two distinct sets of marine transgressive-regressive cycles from the Quaternary sedimentary stratigraphy of the Pearl River Delta (Huang et al., 1982; Zong et al., 2016). However, the timings and spatial extent of the late Quaternary marine transgressions remain contentious, with persistent discrepancies across studies regarding their chronology and distribution (Yim, 1999; Fu et al., 2020b; Huang et al., 2021; Zhou et al., 2022; Lu et al., 2023; Zheng et al., 2023; Yu et al., 2025).

Radiocarbon dating (^{14}C) is the primary chronological tool for the late Quaternary sediments within the past ~55,000 years (Hajdas et al., 2021). However, its applicability is limited for deposits exceeding the age threshold. In contrast, luminescence dating techniques provide robust age constraints for sediments spanning the past 500,000 years or more (Smedley, 2018; Mahan et al., 2022), particularly through recent innovations in measurement protocols and analytical approaches (Buylaert et al., 2009; Buylaert et al., 2012; Li and Li, 2012; Li et al., 2015b; Peng and Li, 2017; Li et al., 2018b; Li et al., 2023). Moreover, luminescence dating has established reliable chronological frameworks for coastal deposits across China (Gao et al., 2016, 2017, 2020, 2021, 2022; Li et al., 2019; Liu et al., 2022b; Riedesel et al., 2018) and globally (e.g., Jacobs, 2008; Kenzler et al., 2015; Lamothe, 2016).

Recent luminescence dating studies (e.g., Xu et al., 2020; Lin et al., 2022b; Xu et al., 2022; Zhong et al., 2022; Lin et al., 2023; Zhong et al., 2023; Liu et al., 2025) have targeted sediments of the Pearl River Delta

and adjacent coast in southern China. While significant advancements have been made in luminescence dating techniques in past decades, including single-aliquot (SA) and single-grain (SG) quartz optically stimulated luminescence (OSL) and K-feldspar (KFS) infrared stimulated luminescence (IRSL) dating techniques (Buylaert et al., 2012; Li et al., 2015a; Peng and Li, 2017; Li et al., 2018; Murray et al., 2021; Long et al., 2025), published luminescence ages for the Pearl River Delta's pre-Holocene stratigraphy remain scarce. Previous work has primarily focused on subaerial delta sections (Xu et al., 2020, 2022; Lin et al., 2022b, 2023; Zhong et al., 2022, 2023) or Holocene sedimentary systems (Zong et al., 2012; Xiong et al., 2018a, 2018b; Xiong et al., 2020; Fu et al., 2020a; Chen et al., 2023). However, sedimentary sequences from the estuary to the South China Sea shelf poorly constrained, a gap that complicates the reconstruction of the Pearl River Delta's sedimentary history. Crucially, understanding the formation age of pre-Holocene marine and terrestrial layers relative to sea-level changes is thus essential for deciphering the delta's evolution. Addressing this chronological deficit requires comprehensive and consistent dating studies to enhance knowledge of the region's past dynamics and climatic responses.

This study aims to establish a reliable chronological framework for the late Quaternary sedimentary stratigraphy in the Pearl River Delta region. We employ an integrated approach combining quartz OSL, SA/ SG KFS luminescence and radiocarbon dating techniques. Analyses focused on sediment samples from Core CP-QZ04, which records significant land-sea interactions. Establishing this chronostratigraphic framework will facilitate regional stratigraphical correlation and comparative studies while providing robust evidence supporting the hypothesis that the Pearl River Delta's depositional evolution has been profoundly influenced by global climate fluctuations and sea-level changes since the late Quaternary.

2. Regional setting

The Pearl River is a major river in East Asia, with a drainage basin covering approximately 450,000 km² and a total length of 2300 km (Huang et al., 1982; Wei and Wu, 2011). It discharges approximately 92×10^6 tons of sediments per year and 330×10^9 m³ of runoff. The Pearl River Delta is situated within a land-sea interaction zone, forming a composite delta characterized by densest channel networks. It was formed by the confluence of the Xi Jiang, Bei Jiang, and Dong Jiang rivers, along with numerous smaller distributaries (Huang et al., 1982). The river's final distributaries flow into the northern continental margin of the South China Sea (Fig. 1). The delta's mouth comprises a complex depositional system with eight major outlets (known as "Men" in Chinese), distributed across three branches: the East River, North River, and West Rivers. Separated by the Wugui Hill, these outlets are grouped as follows: Humen, Jiaomen, Hongqimen, and Hengmen to the east; and Modaomen, Jitimén, Hutiaomen, and Yamen to the west (Wei and Wu, 2011; Lin et al., 2022a).

The Pearl River Delta has a complex evolutionary history, shaped by the combined influence of global sea-level changes, regional tectonic movements, the intricate river network, and a mosaic of terrain including plains, hills, islands, and terraces (Yu et al., 2016). During the late Quaternary, active faulting and uplifting led to an expansion of accommodation space for sediment deposition from semi-enclosed drainage basins, accompanied by alternating marine transgressions and regressions. This resulted in formation of two terrestrial sequences (T1, T2) and two marine sequences (M1, M2) (Fu et al., 2020b; Zong et al., 2009b; Yu et al., 2016). The thickness of the Quaternary sediments

in the Pearl River Delta ranges from 10 to 40 m, with localized deposits reaching up to 60 m in paleovalleys within the Xijiang River and Beijiang River deltas (Huang et al., 1982). The Holocene delta evolution and sequence stratigraphy analyses of the Pearl River Delta reveal that sedimentary sequences within paleovalleys, from the bottom to top, are characterized by fluvial, floodplain-estuarine, and estuarine-deltaic facies. Conversely, sequences on paleo-interfluviums consist of littoral, estuarine, and delta facies, reflecting the history of sea-level change (Wei and Wu, 2011; Xiong et al., 2018). The climate of this region is dominated by warm and humid East Asian monsoon (Strong et al., 2013).

3. Materials and methods

3.1. Core drilling and sediment sampling

In 2019, a 53-m-long borehole core (CP-QZ04; 22°28'13.09"N, 113°37'15.93"E) was retrieved from the Pearl River estuary at a water

depth of ~2.0 m (Fig. 1b). Sediment sampling followed this strategy:

- 1) From the upper section (0–16.8 m): Collected 11 samples for radiocarbon dating (Table S1), 112 samples at 10–15 cm intervals for grain size analysis, and 105 samples at 10–20 cm intervals for diatom analysis (Zhang et al., 2024).
- 2) From the middle section (18–31 m): Extracted eight undistributed 20-cm-long sediment segments (this study, Table 1). These were immediately split, packaged in opaque plastic tubes, and stored for subsequent luminescence dating pretreatment in laboratory. The core was then split lengthwise for sediment descriptions, photography, and further sampling.
- 3) From the middle to lower sections (18.1–51.9 m): Collected 14 sediment samples (this study) at relatively coarse resolution for grain size analysis to confirm lithological variations.

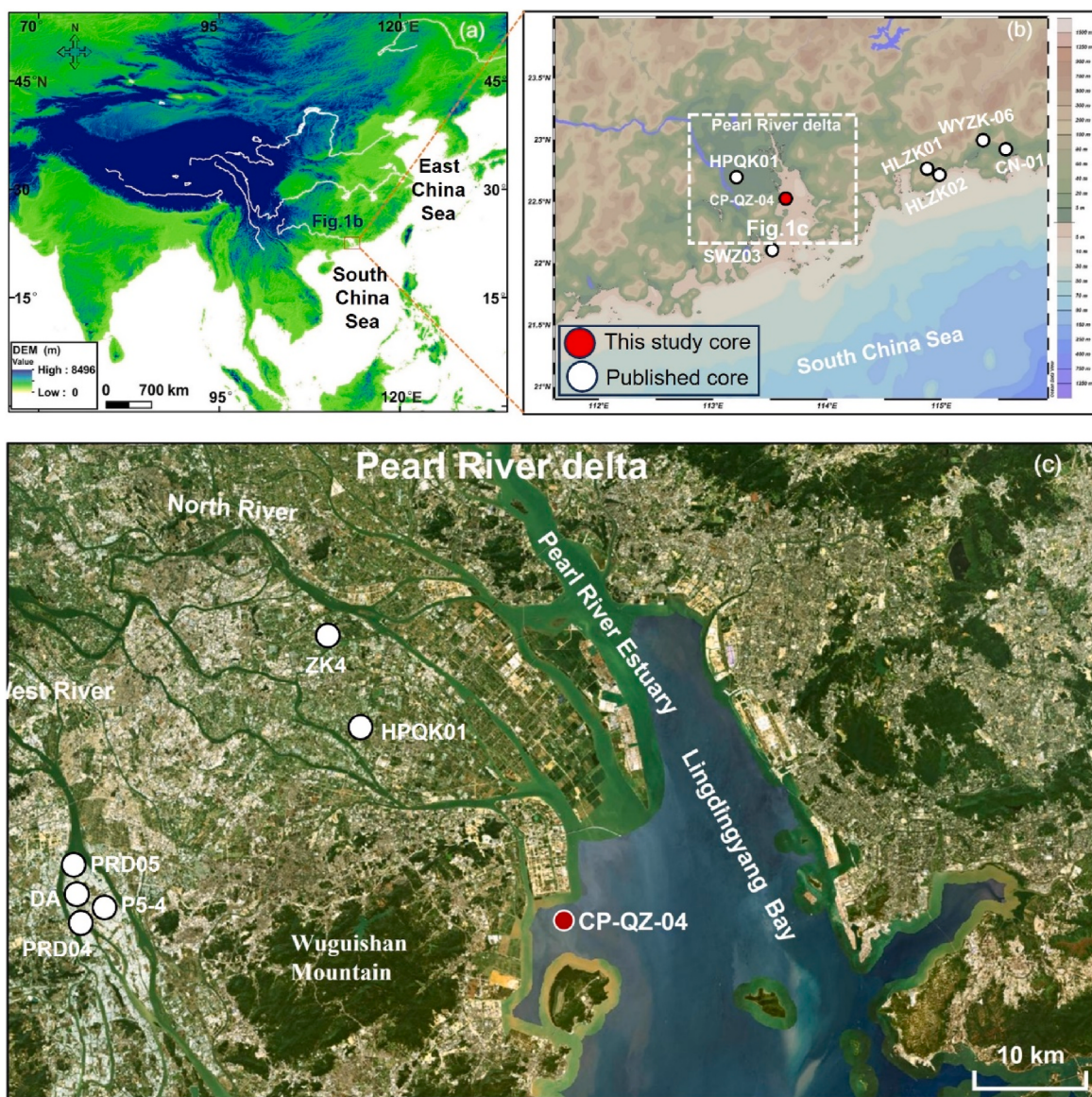


Fig. 1. The map shows the study area and locations of the study core (CP-QZ-04) alongside previously published cores. (a) Geographic position of the Pearl River and its delta within East Asia; (b) Geomorphological, topographic, and bathymetric features of the Pearl River Delta and its adjacent coastal zone; (c) Satellite image (Google Earth) of the Pearl River Delta, with information of the main tributaries and estuary. Previously published cores shown in (b) and (c), includes core HPQK01 (Xu et al., 2022), core SWZ03 (Zheng et al., 2023), core HLZK01 and HLZK02 (Liu et al., 2025), cores PRD05, DA and PRD04 (Lin et al., 2022), core P5-4 (Lin et al., 2023), core ZK4 (Fu et al., 2020b), core WYZK-06 (Song et al., 2012), and core CN-01 (Tang et al., 2018).

Table 1

Dose rates of luminescence dating samples. Qz is the abbreviation of quartz.

Sample ID	Depth (m)	U (ppm)	Th (ppm)	K (%)	Water content (%)	Total dose rate (Gy/ka)			
						CG Qz	FG Qz	PM	KFS
NL-2276	18.1	1.67 ± 0.10	11.2 ± 0.03	1.05 ± 0.00	23.4 ± 10	1.74 ± 0.13	2.16 ± 0.19	2.71 ± 0.19	2.50 ± 0.17
NL-2278	22.4	1.83 ± 0.07	8.41 ± 0.03	0.52 ± 0.00	24.1 ± 10	1.19 ± 0.12	1.54 ± 0.18	2.01 ± 0.18	1.95 ± 0.17
NL-2279	23.1	1.83 ± 0.06	7.76 ± 0.03	0.80 ± 0.00	13.9 ± 10	1.49 ± 0.14	1.87 ± 0.20	2.37 ± 0.20	2.27 ± 0.19
NL-2280	24.1	1.60 ± 0.05	5.79 ± 0.02	2.04 ± 0.01	7.40 ± 10	2.58 ± 0.18	2.97 ± 0.22	3.40 ± 0.22	3.32 ± 0.21
NL-3478	26.1	3.97 ± 0.06	10.7 ± 0.16	1.17 ± 0.04	13.9 ± 10	2.36 ± 0.18	2.97 ± 0.25	3.84 ± 0.25	3.22 ± 0.21
NL-2281	27.1	1.24 ± 0.04	5.03 ± 0.02	2.14 ± 0.01	10.8 ± 10	2.46 ± 0.17	2.78 ± 0.20	3.12 ± 0.20	3.17 ± 0.20
NL-3479	27.7	2.56 ± 0.04	7.62 ± 0.11	0.93 ± 0.03	11.2 ± 10	1.76 ± 0.17	2.78 ± 0.20	2.81 ± 0.23	2.57 ± 0.21
NL-3480	30.7	2.28 ± 0.02	6.17 ± 0.07	0.78 ± 0.02	9.25 ± 10	1.53 ± 0.17	1.90 ± 0.22	2.43 ± 0.22	2.32 ± 0.21

3.2. Sedimentology analysis

To identify sedimentary facies and stratigraphy units of core CP-QZ04 (Fig. 2), the split sediment core was photographed and its characteristics documented. We observed the lithology, color, texture, sedimentary structures (including bedding/lamination), and contact relationships between different layers. Sedimentological analysis of the core photographs was used to identify sedimentary stratigraphy and facies. Representative 30-cm-long sections were then selected from these photographs to illustrate typical sedimentary facies variations throughout core (Fig. 3). Given the similarity of late-Pleistocene-to-Holocene stratigraphy and sedimentary facies sequences across multiple cores in the Pearl River Delta (Wei and Wu, 2011; Chen et al., 2023; Yu et al., 2025), we correlated the stratigraphic architecture of the core with previously defined stratigraphic framework (e.g., Fu et al., 2020b;

Zheng et al., 2023; Chen et al., 2023).

3.3. Grain size analysis

Grain size analyses were performed on representative sediments from core CPQZ-04 using a Mastersizer 3000 laser diffraction particle size analyzer (Malvern Instruments, UK). A total of 14 sediment samples were pretreated as follows: 1) 0.2–0.3 g of sediments was weighed for preparation; 2) organic matter was removed with 10 % H₂O₂ solution; 3) carbonates were eliminated with 10 % HCl; and 4) 10 mL of 0.05 mol/L sodium hexametaphosphate solution was added. Finally, all pretreated samples were analyzed using Mastersizer 3000 analyzer, with each sample measured three times to obtain an average value.

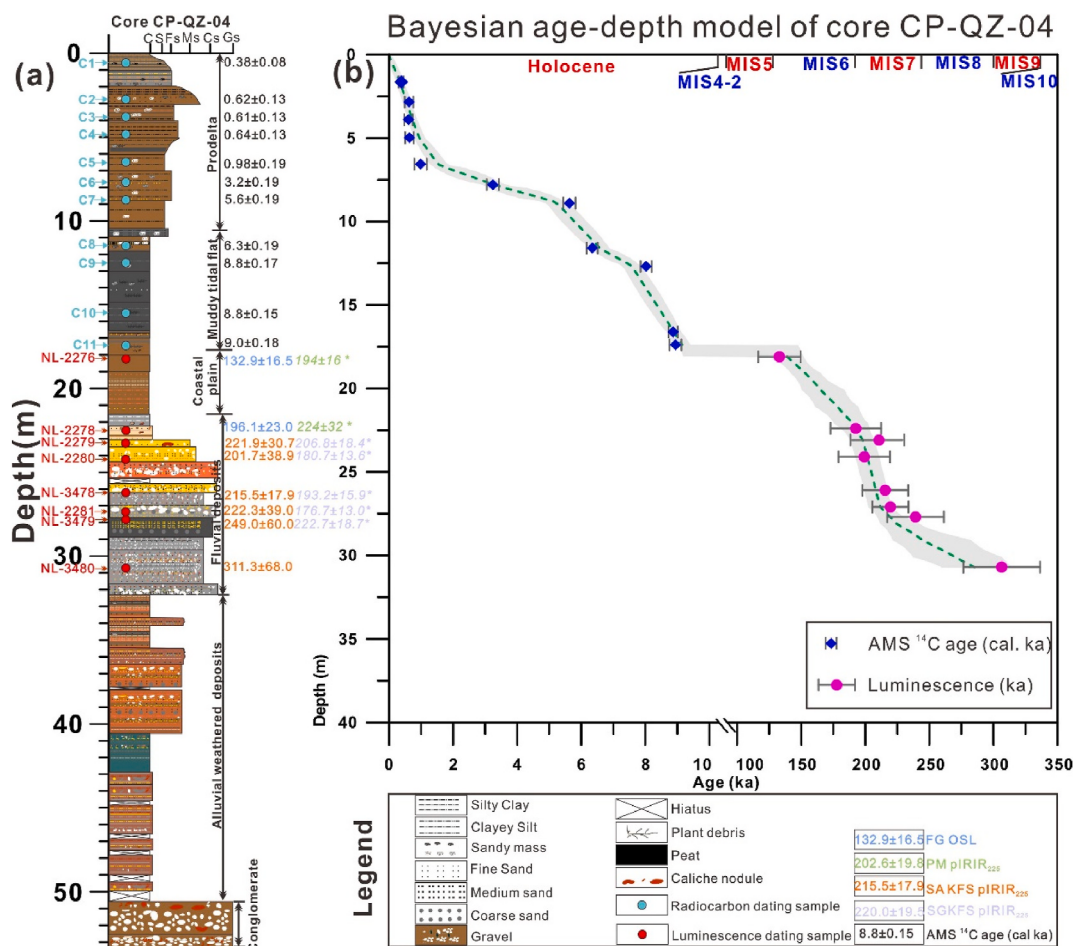


Fig. 2. Lithology and chronostratigraphy of core CP-QZ-04. (a) Sediment lithology, sedimentary facies, depths of radiocarbon and luminescence dating samples, sample ID, and corresponding ages. (b) Bayesian age-depth model of the study core, integrating composite radiocarbon dating (AMS ¹⁴C) and luminescence ages.

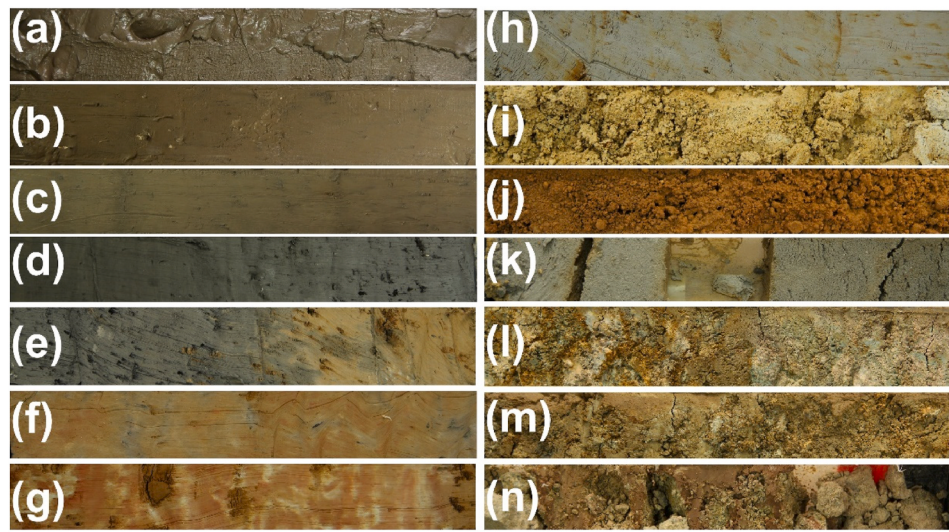


Fig. 3. Representative sedimentary facies and stratigraphy for core CP-QZ04. (a) Deformed soft mud and gray clayey silt in prodelta environments (0.3–0.6 m); (b) Brownish silty clay in prodelta environments (1.5–1.9 m); (c) Brownish to yellowish silty clay (2.2–2.5 m) prodelta environments; (d) Dark gray muddy sediments with sporadic shells in muddy tidal flat depositional environments (13.5–13.8 m); (e) Dark gray to yellowish silt in muddy tidal flat depositional environments (16.5–16.8 m); (f–g) yellowish to reddish weathered homogeneous clay in coastal plain environments (18.2–18.5 m, 19.8–20.0 m); (h) gray to yellowish silt to fine sand in fluvial channel environments (21.7–22.1 m); (i) Massive medium to coarse sand in fluvial channel environments (23.5–23.80 m); (j) Reddish to yellowish-brown sand and gravel in fluvial channel environments (24.7–25.0); (k) Gray to brownish coarse sand in fluvial channel environments (26.4–26.7); (l–n) Yellowish conglomeratic sandstone and weathered paleosol-like deposits in fluvial to alluvial environments (35.8–36.1 m, 43.9–44.2 m, 51.5–51.8 m). (For interpretation of the references to color in this figure legend, the reader is referred to the Web version of this article.)

3.4. Luminescence dating of core sediments OSL and IRSL signals

3.4.1. Pretreatment of luminescence dating sample

Sediment samples in this study were chemically treated using the same workflow as described in our previous studies (Gao et al., 2017, 2021, 2022) to extract target minerals for luminescence dating. Based on the grain size distribution characteristics of the sediments, we isolated coarse-grained quartz (CG, 100–200 μm), fine-grained quartz (FG, 4–11 μm), polymimetic (PM) fractions, and KFS grains.

3.4.2. Protocols and equipment for luminescence dating

In this study, single-aliquot regenerative-dose (SAR) protocols (Murray and Wintle, 2000) were utilized to measure quartz OSL signals. Modified pIRIR₂₂₅ protocols (Buylaert et al., 2009) were applied to polymimetic fractions and multi-grain KFS samples, while the single-grain dating protocols (Long et al., 2024) were employed for SG KFS pIRIR₂₂₅ signals measurements. For individual samples, different luminescence signals or grain sizes were measured using these SAR or SG pIRIR protocols to enable age comparisons and cross-checking. In addition, to avoid potential age underestimation for high-dose sample in D_{es} measurements, this work also evaluated the performance of KFS pIR₂₀₀IR₂₉₀ dating protocols following previous recommendations (Li and Li, 2012). Detailed experimental procedures for quartz OSL, PM/KFS pIRIR₂₂₅, and pIR₂₀₀IR₂₉₀ signals measurements are summarized in Table S2.

To establish suitable measurement conditions for core sediment sample CP-QZ04, this study carried out a series of preliminary tests to ensure the reliability and accuracy of the luminescence dating results. These tests included dose recovery tests (DRTs) and preheat plateau tests (PHTs) for quartz grains, as well as DRTs and residual dose measurements for SG KFS IRSL signals. For the PHTs and DRTs on quartz grains, preheat temperatures were set at 20 °C intervals from 180 °C to 280 °C. The cut-heat temperature for all the measurements was set at minus 20 °C relative to the corresponding preheat temperature. In the DRTs for both quartz and KFS grains, the added doses were set to approximate the equivalent doses (D_{es}) of representative samples. For example, added doses of 331.8 Gy and 411.2 Gy were applied to one FG quartz sample

(NL-2278, $D_{\text{e}} = 331.8$ Gy), and three SG KFS samples (NL-2280, 3489, 3480, $D_{\text{e}} = 411.2$ Gy), respectively. To assess residual doses in the KFS grains, residual dose tests were conducted on two representative samples (NL-2280 and NL-3478) using the SG dating protocols. Prior to residual dose measurement, one aliquot containing 100 grains was prepared for each sample. These aliquots were then bleached for 4 h in an artificial sunlight stimulator (Hönle SOL2).

D_{es} of all samples were determined using the procedures outlined in Table S2. For SA quartz OSL and KFS pIRIR₂₂₅ D_{es} determinations, the following acceptance criteria were applied during data selection (Gao et al., 2020): 1) The natural test dose signal (T_n) must exceed the background (BG) by at least 3 standard deviation (3σ); 2) Recuperation (% of N) must be less than 5 % of the natural signal (N); 3) The maximum palaeodose error must be less than 20 %; 4) The maximum test dose error must be less than 10 %; 5) The recycling ratio must be within 10 % of unity. For SG KFS D_{e} data selection, the following criteria were considered: (1) The initial T_n signal must be less than 3 times the standard deviation of its corresponding background signal; (2) The recycling ratio must not differ from unity by more than 2 σ ; (3) Recuperation must not exceed 10 %; (4) The figure of merit (FOM) must not exceed 10 % (Peng and Li, 2017); and (5) The \ln/T_n value must not surpass the saturation level of the dose response curve. The data filtering process described above, as well as the determination of SG D_{e} values, were performed using the “numOSL” R package (Peng et al., 2013; Peng and Li, 2017).

Anomalous fading rates of the targeted samples' IRSL signals were measured following Auclair et al. (2003). Fading corrections were applied to the age using the models of Huntley (2006), as proposed in Kars et al. (2008).

All measurements were performed on Risø TL/OSL-DA-20-D automated readers at the Luminescence Dating Laboratory of the Nanjing Institute of Geography and Limnology, Chinese Academy of Sciences (NIGLAS).

3.4.3. D_{e} distribution and statistical analysis using central age model

To characterize the distribution and overdispersion of SA and SG KFS pIRIR₂₂₅ D_{es} values, statistical analysis using central age models

(Galbraith et al., 1999; Galbraith and Roberts, 2012; Liang and Forman, 2019) were conducted for age calculation.

3.4.4. Dose rate and luminescence age calculation

For dose rate determination, the concentrations of Uranium (U) and Thorium (Th) elements in five samples (NL-2276, 2278–2281) were measured by inductively coupled plasma mass spectrometry (ICP-MS), while potassium (K) concentration in these samples were determined via inductively coupled plasma-optical emission spectrometry (ICP-OES) at Nanjing University. For the remaining three samples (NL-3478–3480), concentrations of the radioactive nuclides ^{238}U , ^{232}Th , and ^{40}K were measured using a Risø NaI gamma spectrometer in the Luminescence Dating Laboratory at School of Geography, Nanjing Normal University.

The total dose rates of all samples were calculated considering the concentrations of natural radionuclides, including U, Th, and K, as well as water content, burial depth, altitudes, and geomagnetic latitudes of each sample (Prescott and Hutton, 1994; Aitken, 1998). We integrated these parameters into the calculation (Bell, 1979; Mejdahl, 1979; Balescu and Lamothe, 1994; Huntley and Baril, 1997; Adamiec and Aitken, 1998; Guérin et al., 2011), following the methodology described in our previous studies dating coastal sediment core (Gao et al., 2021, 2022). Considering the alpha efficiency, we adopted the following α -values to estimate the external alpha-ray dose rates: 0.04 ± 0.02 for FG quartz (Mauz et al., 2006), 0.08 ± 0.02 for PM (Rees-Jones, 1995), and 0.15 ± 0.05 for KFS (Balescu and Lamothe, 1994). For the internal dose rate calculations in KFS, we assumed a potassium (K) concentration of $12.5 \pm 0.5\%$ and a rubidium (Rb) concentration of 400 ± 100 ppm (Huntley and Lamothe, 2001). Finally, the luminescence ages for each dosimeter types, including SA quartz, PM grains, and SA/SG KFS grains, were determined by dividing their respective D_e values by the corresponding total dose rate.

4. Results

4.1. Sedimentary facies and stratigraphy of core CP-QZ04

The sedimentary stratigraphy of the study core (Fig. 2) comprise the following units: conglomerate-based fluvial-channel deposits (53–51 m), weathered alluvial deposits (51–32.5 m), fluvial-channel deposits (32.5–22 m), coastal plain (22–17 m), muddy tidal-flat deposits (17–10 m), and prodelta deposits (17–0 m). These sedimentary facies were defined based on observed characteristics within core intervals (Fig. 3a–n), and regional late Quaternary stratigraphic framework established in previous studies (Fu et al., 2020b; Wei and Wu, 2011; Xing and Yu, 2011; Huang et al., 2021; Lu et al., 2023; Zheng et al., 2023). The sedimentary features of each sedimentary facies, as observed in typical layers, are briefly described below:

The prodelta sedimentary stratigraphy comprised deformed soft mud and gray clayey silt (0.3–0.6 m, Fig. 3a), brownish silty clay (1.5–1.9 m, Fig. 3b), and brownish to yellowish silty clay (2.2–2.5 m, Fig. 3c). The muddy tidal flat stratigraphy features dark gray muddy sediments with sporadic shells (13.5–13.8 m, Fig. 3d) and dark gray to yellowish silt (16.5–16.8 m, Fig. 3e). Coastal deposition is characterized by yellowish to reddish weathered homogeneous clay (e.g., 18.2–18.5 m, 19.8–20.0 m, Fig. 3f and g). Fluvial-channel dominated sedimentary successions consist of: gray to yellowish silt to fine sand in the upper layers (21.7–22.1 m, Fig. 3h); massive medium to coarse sand in the middle layers (23.5–23.8 m, Fig. 3i); and reddish to yellowish-brown sand and gravel in the lower layers (24.7–25.0 m, Fig. 3j), overlain by gray to brownish coarse sand (26.4–26.7 m, Fig. 3k). Between 26.7 and 35.8 m depth, the sediments transition from gray coarse sand to reddish/yellowish-brown sand and gravel, showing reduced structural organization. The basal stratigraphy comprises yellowish conglomeratic sandstone and yellowish to reddish weathered paleosol-like deposits, typical of fluvial to alluvial environments, found at 51.5–51.8 m, 43.9–44.2 m, 35.8–36.1 m (Fig. 3n–l).

4.2. Grain size distribution of core sediments from typical stratigraphy

As shown in Fig. 4, sediments from typical layers and units (Fig. 2) representing fluvial, alluvial, coastal plain, and tidal flat environments exhibit distinct modes in their grain size distributions. For instance, sediment samples from fluvial units (e.g., 51.9 m, 31.7 m, 23.1 m) show two or three peaks and have relatively high mean grain size ($>100 \mu\text{m}$), suggesting heterogeneous deposition in high-energy hydrodynamic environments. In contrast, sediments collected from the coastal plain (18.1 m, 22.4 m) and alluvial weathered stratigraphy (40.5 m) within this core display relatively narrow distribution with smaller mean values ($<50 \mu\text{m}$). Additionally, the grain size characterizations of the upper 18 m of this same core were previously analyzed in another study (Zhang et al., 2024). Overall, the sediment grain size characteristics and their distributions are consistent with core lithology observations and loggings (Figs. 2–4).

4.3. Quartz OSL, PM, and KFS pIRIR₂₂₅ dating of the Pearl River Delta core sediments

4.3.1. Characteristics of different luminescence signals

This study first examined luminescence characteristics of quartz OSL signals, PM fractions and KFS pIRIR₂₂₅ signals from core sediments prior to D_e measurements. As shown in Fig. S1, the luminescence signals (L_n , L_x) and thermoluminescence (TL) signals of CG quartz OSL are very weak or dim. This suggests that CG quartz luminescence signals from this core are not suitable for further luminescence dating. In contrast, the dose response curves and decay curves of FG quartz OSL signals, CG KFS and FG PM pIRIR₂₂₅ signals exhibit quite normal shape (Fig. 5a–c), supporting the feasibility of using these signals for subsequent luminescence dating of this core sediments. The behavior of the SG KFS pIRIR₂₂₅ signals shown in Fig. 5d is normal, indicating suitability for D_{es} estimation. Overall, the characteristics of different luminescence signals (FG quartz OSL, PM, and SA/SG KFS pIRIR₂₂₅) suggest that they are suitable for D_{es} measurements, with exception of CG quartz OSL signals.

4.3.2. Performances of luminescence dating signals in pretests

As shown in Fig. 5e and f, the results of the PHTs and the DRTs conducted within SAR protocols indicate that preheat temperatures of 260 °C for 10 s, followed by a cut-heat temperature of 240 °C, are more suitable for OSL dating of FG quartz grains from the study core sediments. This conclusion is supported by a series of criteria, including low recuperations ($<5\%$), satisfactory recycling ratios (0.9–1.1), and dose recovery ratios (0.9–1.1). In Fig. 6a, the DRT values obtained using the SG KFS pIRIR₂₂₅ protocols for three samples (NL-2280, 3478, and 3480) from different layers fall within the range of 0.9–1.1, indicating that the SG KFS pIRIR₂₂₅ dating protocols performs well for this study. Residual doses for two representative samples (NL-2280 and NL-3478) range from 5 to 20 Gy, with averages of 10–11 Gy (Fig. 6b). These values are significantly lower than their corresponding D_e values. Overall, the performance of DRTs and the magnitude of residual doses of KFS pIRIR₂₂₅ signals from several representative samples suggest that the modified pIRIR₂₂₅ protocols are feasible for determining KFS D_e values of sediments from the present Pearl River Delta estuary region.

4.3.3. D_{es} distribution, dose rates, and luminescence age calculations

The D_{es} distributions of FG quartz grains for two representative samples (NL-2276 and NL-2278, Fig. 7) cluster within 290–300 Gy, averaging values around 300 Gy. However, the FG quartz D_{es} for sediment samples from the middle to lower sections of core CP-QZ04 may be underestimated due to OSL signals saturation as suggested by the results from a comparison of D_e values versus D_0 values (Fig. S2). In contrast, the PM fractions and KFS pIRIR₂₂₅ D_{es} provide more robust age estimates (Fig. 5b–d). The SA and SG KFS pIRIR₂₂₅ D_e values for all dating samples are shown in Fig. 7. These D_e values range from 400 to 700 Gy and exhibit distribution close to normal. As reported in previous studies, the

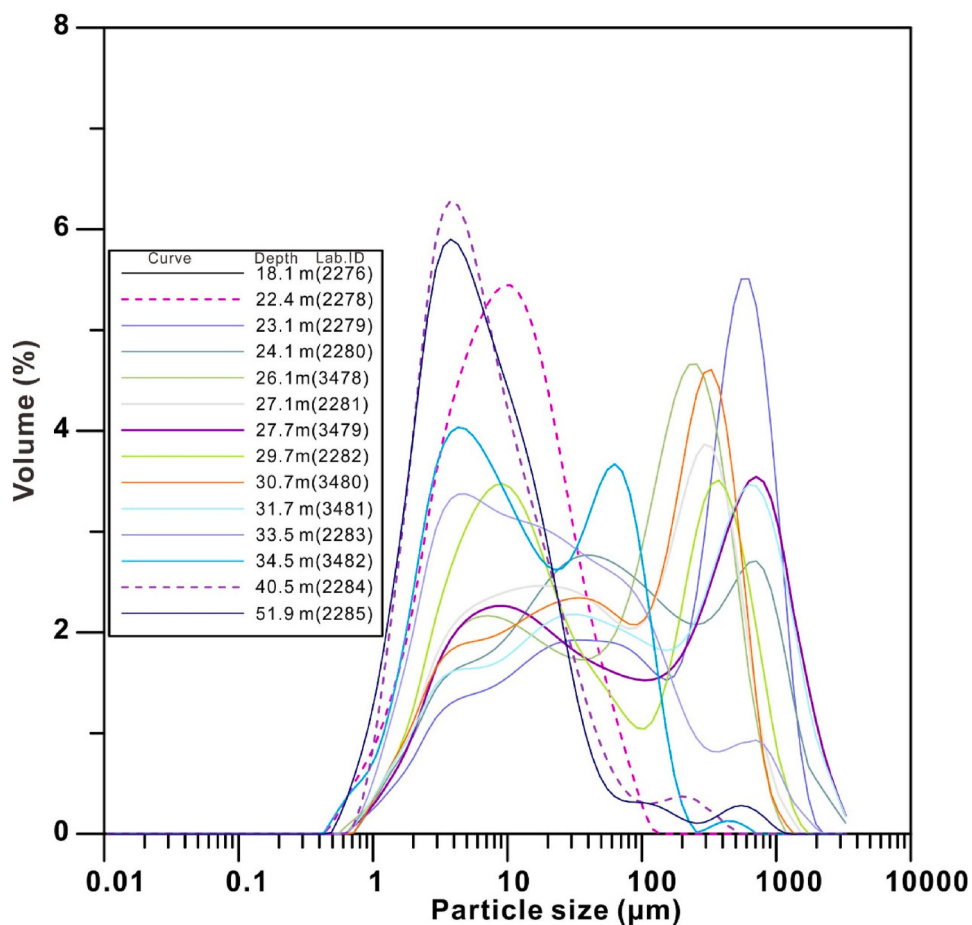


Fig. 4. Grain size distribution of different sedimentary layers in core CP-QZ04.

SG approach has an advantage in identifying incomplete bleaching of luminescence signals (Duller et al., 2008; Smedley et al., 2019). The D_e distributions in Fig. 7 suggest that the KFS grains were generally completely bleached, making them suitable for establishing age control for the core sediments.

The dose rates of each sample associated with their corresponding radioactive elements of U, Th, K, and associated water contents, are shown in Table 1. Overall, the dose rates for all measured materials, including CG and FG quartz grains, PM fractions and KFS grains, vary in the range of 1.5–3.8 Gy/ka. Quartz grains dose rates are consistently below 3 Gy/ka, while those of PM and KFS grains are typically around 3 Gy/ka.

Based on the D_{eS} values measured from different luminescence signals and their corresponding dose rates, the determined luminescence ages for the study interval spanning 18.1–30.7 m depth are in the range of 130~300 ka. The D_{eS} values, dose rates, and luminescence ages for all samples are listed in Tables 1–3.

However, SG ages exhibit systematic underestimation compared to SA ages. This discrepancy may arise from two reasons: (1) Some dim KFS grains may yield underestimated D_e values; (2) grains with the largest D_e values were excluded due to signal saturation. The issue of dim grains underestimating D_e can often be resolvable by correlating D_e with grain brightness (Gao et al., 2020). Fig. 8 clearly shows that KFS SG D_e variations are closely dependent on the Tn threshold values. Furthermore, Fig. 9 reveals a component of grains with low ages; the proportion of these grains increase with grain brightness and contributes to higher overdispersion (OD). We analyzed the relationship between SG KFS luminescence dating results for one representative sample (NL-2281) and variations in its Tn thresholds (Fig. S3). The results indicate that D_e values and ages calculated using the brightest 30%–70% of KFS grains

are comparable with their SA counterparts. Fig. S4 shows the light sum curves of pIRIR₂₂₅ signals for all samples. On average, the brightest 54% and 70% of KFS grains contribute 80% and 90% of the total pIRIR₂₂₅ signals, respectively. This suggests that selecting appropriate Tn thresholds can prevent the underestimation of d SG pIRIR₂₂₅ D_e values caused by dim grains, consistent with previous reports (Gao et al., 2020; Wang et al., 2022). Consequently, we selected the final SG KFS ages based on specific Tn thresholds (30%–70%), determined using the relationship between light sum and the proportion of grains (Fig. S4). These refined SG ages are generally consistent with the corresponding SA ages (Table 2).

4.4. Anomalous fading of IRSL signal and age correction

For IRSL dating, anomalous fading is a universal phenomenon (Wintle, 1973). Although the fading effect is negligible for young samples, it might cause significant age underestimation in old samples. A few studies have found that the pIR₅₀IR₂₉₀ signal underestimated the ages of samples with D_{eS} exceeding 400–500 Gy by approximately 10% (e.g., Li and Li, 2012). To assess fading in this study, we measured the anomalous fading rate (g-value) of PM and KFS grains. The g-values of pIRIR₂₂₅ signals for polymineral (p.m.) samples are $2.16 \pm 0.89\%$ /decade and $1.98 \pm 1.05\%$ /decade (Fig. 10a and b). Consequently, the fading-corrected ages of these 2 p.m. samples are 194 ± 26 ka and 224 ± 32 ka (Fig. 11a and b). However, these corrected ages appear overestimated when compared to their FG OSL ages and the uncorrected pIRIR₂₂₅ ages (Table 2). The uncorrected pIRIR₂₂₅ ages are broadly consistent with their OSL age counterparts, suggesting that FG quartz OSL ages might be more reliable ages in constraining on these intervals. In contrast, the g-values of KFS pIRIR₂₂₅ signals (samples

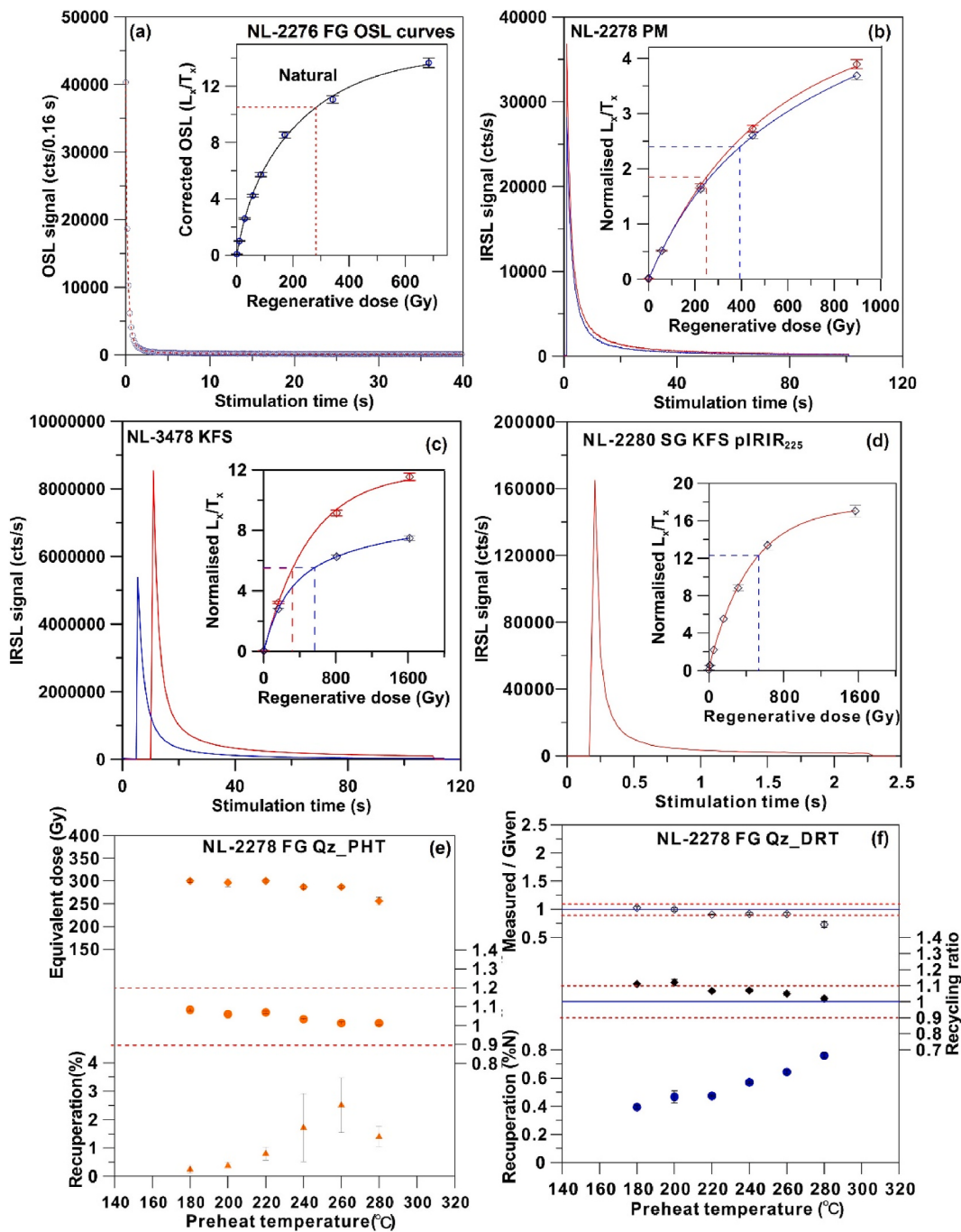


Fig. 5. Characteristics of different luminescence dating signals. (a–d) decay curves and dose response curves of FG quartz OSL, PM fractions, SA, and SG KFS pIRIR₂₂₅ signals from representative samples. (e–f) The results of preheat plateau tests and dose recovery tests for representative FG quartz samples (NL-2278).

NL-2279~2281 and NL-3478~3480) are significantly lower, ranging from $0.57 \pm 0.79\%$ /decade to $1.50 \pm 0.96\%$ /decade (Fig. 10). Accordingly, their fading-corrected ages are listed in Table 2, and these KFS ages (Fig. 11c–h) were employed to establish the chronology of the study core.

4.5. Age-depth model of core CP-QZ04

Considering the characteristics of different luminescence signals, dating uncertainties, the consistency among age results from the same samples, and the principle of stratigraphic sequence, we identified acceptable age components to establish the chronological framework. Based on integrated luminescence dating results from this study and

previously published radiocarbon data for the upper section (1.64–17.38 m) of the same core (Table S1; Zhang et al., 2024), we have established a robust chronological framework spanning ~311 kyr for the present Pearl River Delta estuarine sedimentary sequence (Fig. 2b and Tables 2 and 3). The combined application of these complementary dating techniques significantly enhance chronological control, particularly for the middle to lower core sections where radiocarbon dating lacks sufficient age range for stratigraphic constraints. This refined Bayesian age-depth model provides critical temporal constraints for future studies of late Quaternary sedimentary dynamics of the Pearl River Delta, including quantification of deposition rates, identification of hiatuses, and correlation of regional stratigraphic patterns.

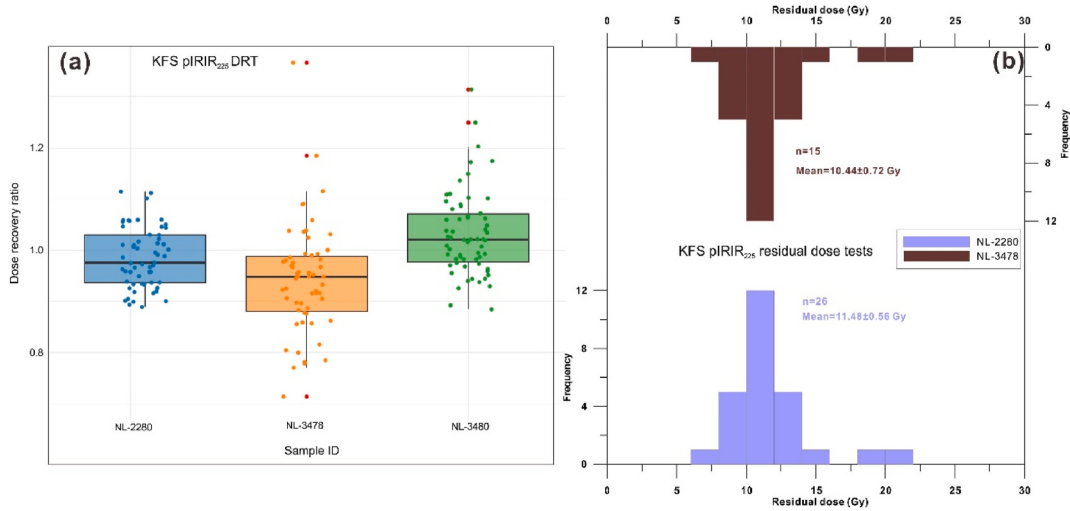


Fig. 6. (a) DRTs and (b) residual dose determination of SG KFS pIRIR₂₂₅ signals.

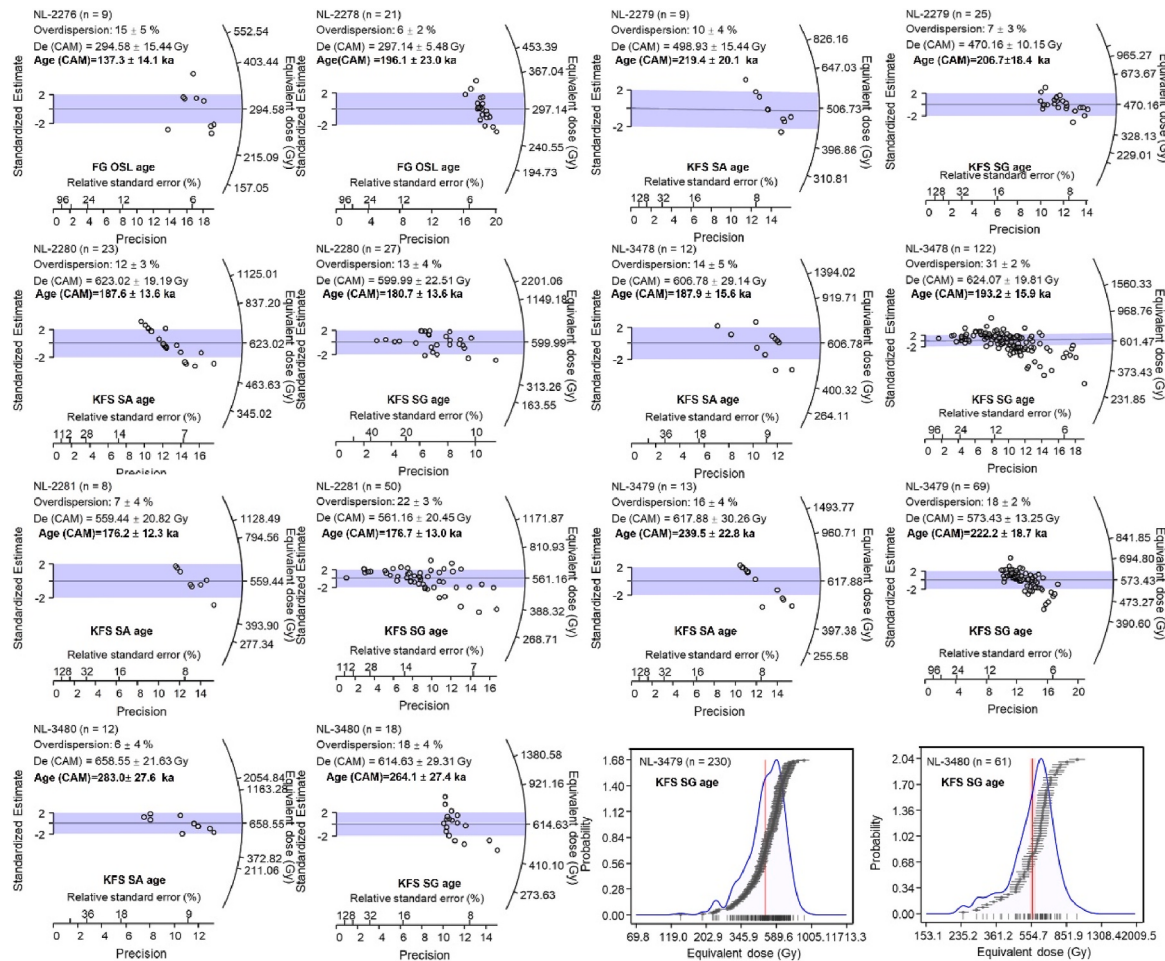


Fig. 7. D_e distribution analysis of core sediments, including: CAM D_e distributions for two FG quartz OSL; CAM D_es values for six SA/SG KFS pIRIR₂₂₅ dating samples; probability density distribution (PDF) for two SG KFS samples.

5. Discussion

5.1. The suitability of the pIRIR dating procedures for the study core sediments

When determining sediment ages across different ranges using IRSL

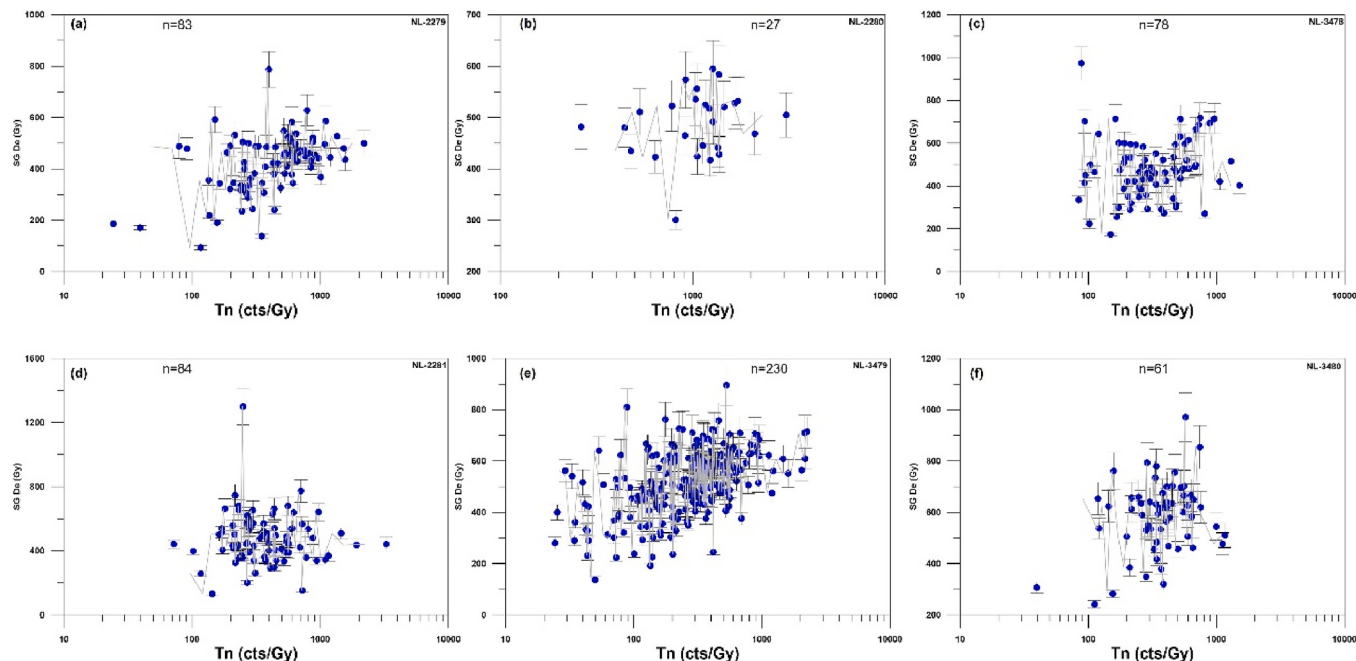
signals, establishing a balance between the stability of the luminescence (e.g., anomalous fading) and bleachability (residual doses) of these signals (Kars et al., 2014) is crucial. According to previous studies (Li and Li, 2012; Li et al., 2014), the pIR₅₀IR₂₉₀ signal may underestimate sample ages by approximately 10 % when D_e exceeds 400–500 Gy (Li et al., 2014). Based on previous findings, the pIRIR₂₂₅ signal may

Table 2Luminescence age of sediment samples from FG quartz OSL and PM pIRIR₂₂₅ dating.

Sample ID	Depth (m)	Equivalent dose (Gy)			Luminescence age (ka)		
		FG Q _e D _e	PM D _e	FG Q _e age	PM age	PM fading-corrected age	Accept
NL-2276	18.1	294.6 ± 15.4	461.9 ± 18.4	137.3 ± 14.1	169.9 ± 13.8	194 ± 16	137.3 ± 14.1
NL-2278	22.4	297.1 ± 5.5	408.3 ± 15.8	196.1 ± 23.0	202.6 ± 19.8	224 ± 32	196.1 ± 23.0

Table 3D_e, OD, and luminescence ages of SA/SG KFS from pIRIR₂₂₅ signals. OD is the abbreviation of Overdispersion. For n/N, N stands for the number of all measured grains using the SG pIRIR₂₂₅ procedures, while n stands for the number of accepted grains passing the SG data selection criteria.

Sample ID	Depth (m)	Equivalent dose (Gy)					Luminescence age (ka)			
		OD _{SA} (%)	KFS SA D _e	(n/N) _{SG}	OD _{SG} (%)	KFS SG D _e	KFS SA age (uncorrected)	KFS SA age (corrected)	KFS SG age	Accept
NL-2279	23.1	10 ± 4	498.9 ± 15.4	25/200	7 ± 3	470.2 ± 10.2	219.0 ± 20.1	221.9 ± 30.7	206.8 ± 18.4	221.9 ± 30.7
NL-2280	24.1	12 ± 3	623.0 ± 19.2	27/100	13 ± 4	600.0 ± 22.5	187.6 ± 13.6	201.7 ± 38.9	180.7 ± 13.6	201.7 ± 38.9
NL-3478	26.1	12 ± 5	606.8 ± 29.1	122/200	31 ± 2	624.1 ± 19.8	187.9 ± 15.6	215.0 ± 30.0	193.2 ± 15.9	215.5 ± 17.9
NL-2281	27.1	7 ± 4	559.4 ± 20.8	50/200	22 ± 3	561.2 ± 20.5	176.2 ± 12.3	222.3 ± 39.0	176.7 ± 13.0	222.3 ± 39.0
NL-3479	27.7	16 ± 4	617.9 ± 30.3	69/400	18 ± 2	573.4 ± 13.2	239.5 ± 22.8	249.0 ± 60.0	222.7 ± 18.7	249.0 ± 60.0
NL-3480	30.7	6 ± 4	658.6 ± 21.6	18/300	18 ± 4	614.6 ± 29.3	283.0 ± 27.6	311.1 ± 68.0	264.0 ± 27.4	311.3 ± 68.0

**Fig. 8.** (a–f) Relationship between individual SG D_e value and intrinsic brightness (quantified via Tn signal intensity, cts/Gy) for six samples. Gray lines indicate moving average across 3-data-point window.

underestimate ages for 200–300 ka samples, due to anomalous fading. To address this issue, two potential approaches are effective: 1) using higher-temperature signals, such as the pIR₂₀₀IR₂₉₀ signals, which exhibit minimal anomalous fading in well-bleached loess samples in northern China (Li and Li, 2012). High preheat and stimulation temperatures can effectively eliminate unstable component and enhance athermal stability; 2) applying fading corrections to adjust the faded ages.

In this study, we evaluated the performance of higher-temperature pIR₂₀₀IR₂₉₀ signals for the core sediments. However, these protocols yield unsuitable dating results for the coastal water-lain deposits, as evidenced by Fig. S5 and S6. The pIR₂₀₀IR₂₉₀ signals exhibited slower decay (Fig. S5), with nearly all KFS samples approaching dose-response curves saturation. Additionally, the dose recovery ratios were systematically overestimated (Fig. S6), suggesting that these high temperature

signals likely result in D_e overestimation in such samples. Recently, Zhao et al. (2025) employed SG K-feldspar pIR₅₀IR₂₂₅ and pIR₂₀₀IR₂₇₅ signals for dating younger (<20 ka) and the older sediment samples from central-southern Plateau paleo-shorelines, respectively. They found that the pIR₅₀IR₂₂₅ signals passed internal reliability tests satisfactorily, however, the pIR₂₀₀IR₂₇₅ protocol showed significant dose recovery overestimation. Furthermore, natural signals from some older grains reached saturation in their dose-response curves, preventing reliable D_e determination and resulting in incomplete SG D_e distributions. Similarly, previous studies have reported that high-temperature stimulated signals exhibit poor bleachability, resulting in elevated residual doses (Kars et al., 2014; Zhang et al., 2015, 2023). This phenomenon is particularly pronounced in water-lain sediments, especially fluvial sediments. For example, Lowick et al. (2012) demonstrated that while pIRIR₂₂₅ ages showed good agreement with independent chronology for

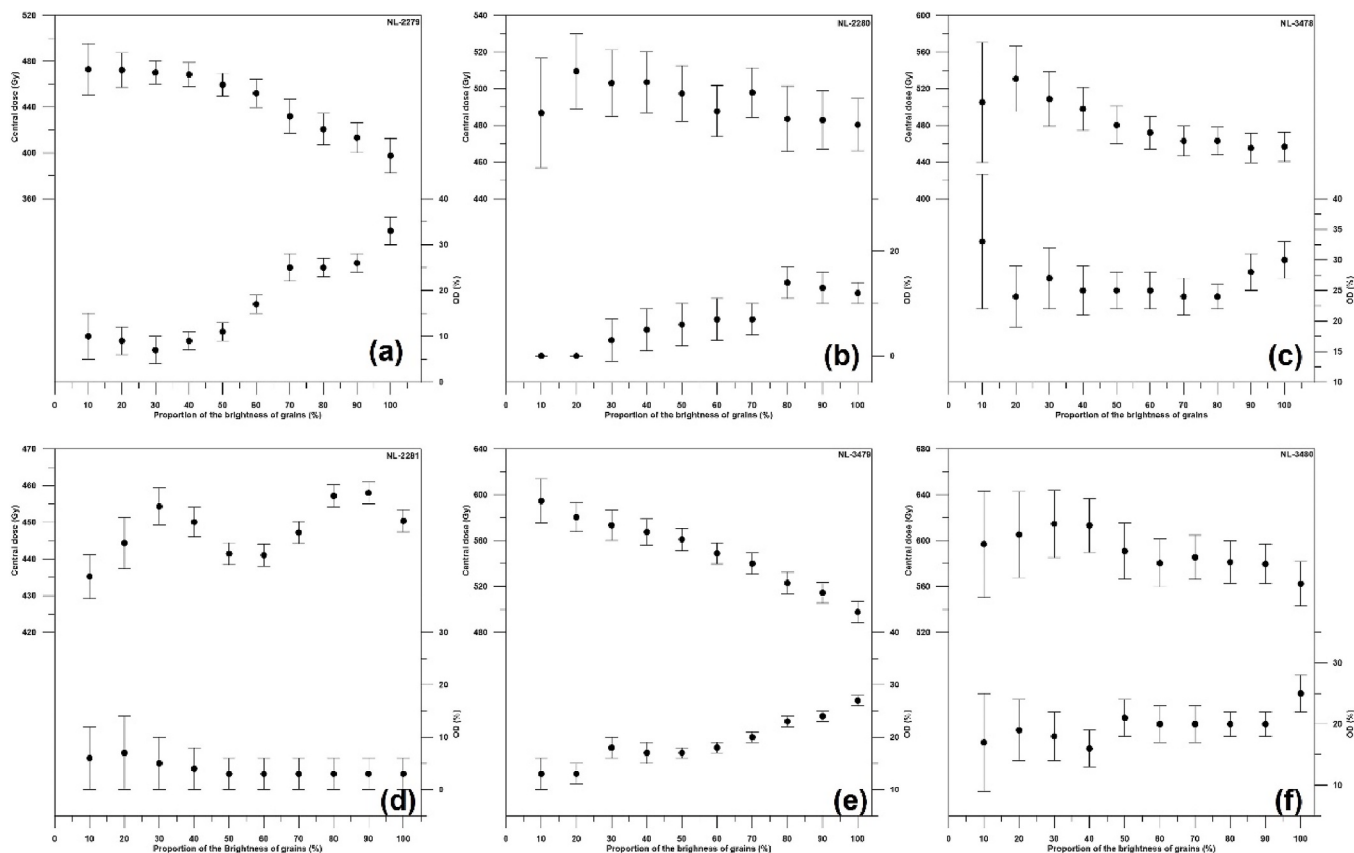


Fig. 9. (a–f) Dependence of CAM D_e and OD values for each sample against the proportion of the brightness of KFS grains.

Swiss fluvial sediments, pIRIR₂₉₀ protocols produced significantly overestimated ages. Thus, the high-temperature protocols (e.g., pIR₂₀₀IR₂₉₀) were temporarily not performed on further measurements for core sediments.

In contrast, the pIRIR₂₂₅ signals demonstrated robust performance for core samples in this study, as evidenced by successful dose recovery tests, low residual dose (Fig. 6), and relatively low anomalous fading rates in KFS grains (Fig. 10). Thus, this study opts to select the lower-temperature pIRIR₂₂₅ protocols (Table S2) for sediment age determination. This approach effectively mitigates the adverse effects observed with higher-temperature signals, where preheat can compromise mineral sensitivity and induce initial sensitivity changes in KFS pIRIR signals (Qin et al., 2018). Moreover, this strategy provides reliable age estimations for the stratigraphy, yielding at least minimum age constraints.

5.2. The reliability of chronology sequence of core CP-QZ04

The radiocarbon ages of upper core sections (~17.38 m; Table S1) reported by Zhang et al. (2024) constrain the timing of Holocene deposits (~9–0.3 cal kyr BP) in the Pearl River Delta estuary. Using these data, we compared the Holocene chronostratigraphy of the estuary with adjacent records, including borehole data from southern (Liu et al., 2008; Xu et al., 2020; Wei and Wu, 2011; Lin et al., 2023), central (Zong et al., 2012; Fu et al., 2020b), head area (Fu et al., 2020a; Xiong et al., 2020b), and northern subaerial sub-deltas (Zong et al., 2009b, 2012; Xiong et al., 2018a; Xu et al., 2022), the Pearl River subaqueous delta on the northern South China Sea shelf (Xiong et al., 2020a; Chen et al., 2023), and coastal plains of the Longjiang (Liu et al., 2025), and Lian Rivers (Song et al., 2012; Tang et al., 2018). For instance, previous studies have proposed evolutionary models of the Holocene Pearl River Delta and shoreline variations based on sediments ages and sea-level

reconstructions (e.g., Zong et al., 2009a; Xiong et al., 2018a, 2018b). The Holocene chronology of core CPQZ-04 aligns well with this established chronological framework. Regional chronostratigraphic correlations across representative boreholes demonstrate that the depositional sequences are generally consistent with previously documented Holocene chronologies in Southern China's coastal regions (Fig. 12).

However, the pre-Holocene chronostratigraphy in the Pearl River Delta region remains poorly constrained, with only a few cores provided limited luminescence age controls (e.g., Xu et al., 2020; Xu et al., 2022; Lin et al., 2022; Lin et al., 2023). Moreover, the robustness of existing chronological framework has not been rigorously verified through independent dating methods, and some discrepancies persist among previous records (Zong et al., 2016; Fu et al., 2020b; Zheng et al., 2023; Lu et al., 2023; Yu et al., 2025).

The reliability of the newly obtained luminescence ages (132–311 ka) for the middle to lower sections of the study core (18–30.7 m; Fig. 2) is supported by multiple lines of evidence. As detailed in Sections 4.3–4.4 and Figs. 5–11, this study conducted a series of pretests to establish optimal measurement conditions for luminescence dating protocols. These tests were critical for validating the experimental procedures and ensuring the robustness of the dating results. For instance, the DRTs (Fig. 6a and S5) were used to evaluate the precision of dose measurements, preheat plateau tests (Fig. 5e and f) helped to determine the optimal preheating temperature for signal stability, and residual dose measurements (Fig. 6b and S7) for different luminescence signals (Fig. 5 and S5) assessed potential unbleached residual signals. Additionally, statistical analysis of KFS pIRIR₂₂₅ D_e distributions revealed relatively low overdispersion values (6–31%; Table 2) when analyzed using the CAM (Galbraith et al., 1999; Galbraith and Roberts, 2012), suggesting relatively homogeneous bleaching prior to burial (Fig. 7). Besides, to investigate the discrepancy between SA and SG KFS ages, this study examined the relationship between SG KFS ages and the Tn thresholds,

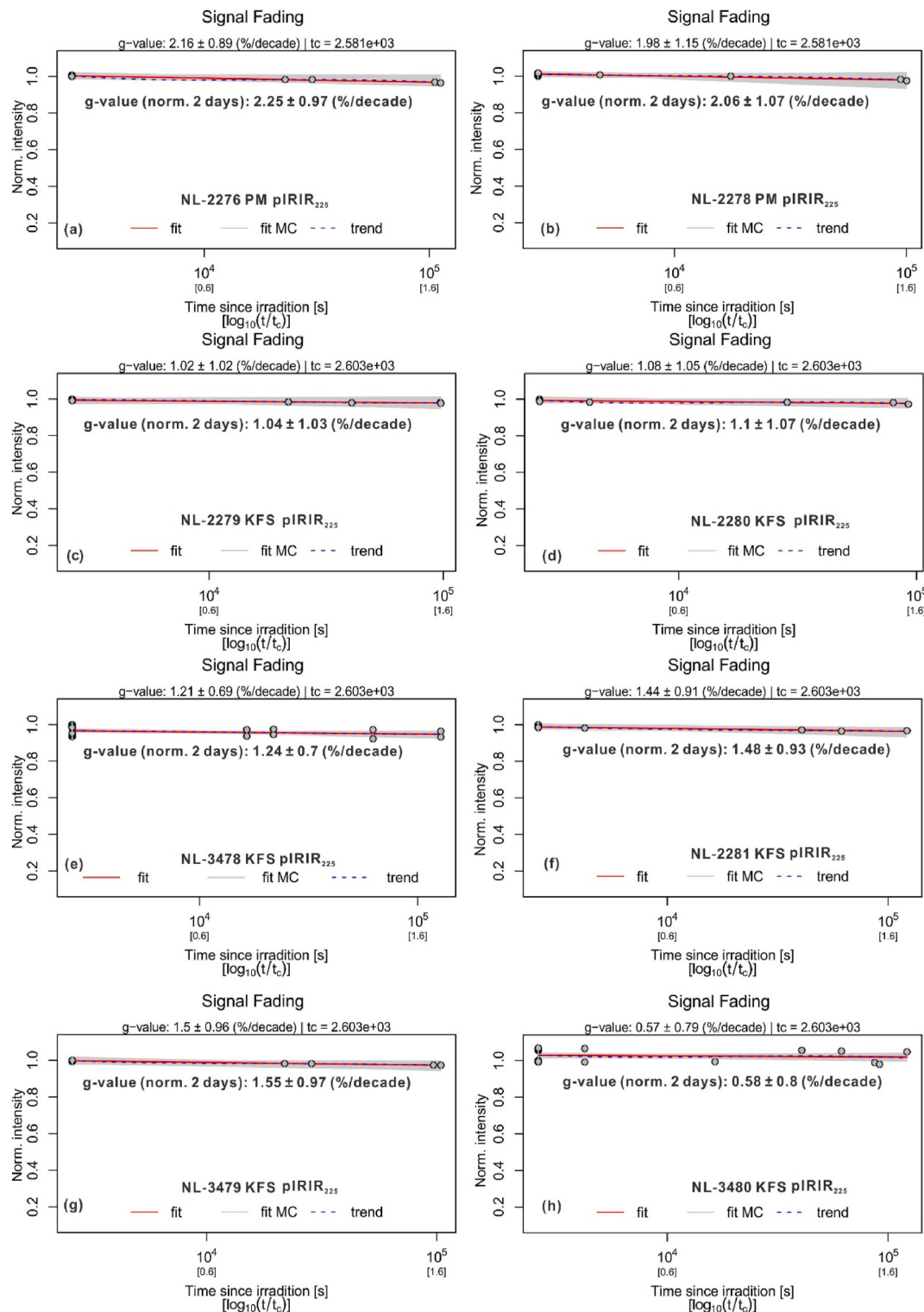


Fig. 10. (a-h) Anomalous fading rates (*g*-value) of PM and KFS grains pIRIR₂₂₅ signals.

by analyzing De-Tn plateaus (Gao et al., 2020, Figs. 8 and 9 and S3) and the correlation of cumulative light sum and the proportion of grains (%) (Reimann et al., 2012; Fig. S4). Additionally, to mitigate potential KFS age underestimation caused by anomalous fading, this study measured the anomalous fading rates (Fig. 10) and applied the fading correction models (Huntley, 2006; Kars et al., 2008) to adjust the KFS ages of core sediments (Fig. 11). Overall, rigorous internal checks of luminescence characteristics across different luminescence signals support the

reliability of the luminescence dating results for core sediments.

Besides, the calculated ages exhibit strong stratigraphic consistency, with minimal age inversions observed in the vertical profile of core CP-QZ04 (Fig. 2). Furthermore, for the same samples, ages derived from different signals remain consistent within 2σ uncertainties (Tables 2 and 3). These findings are further supported by regional chronostratigraphic correlations (Fig. 12). The pre-Holocene chronology sequence obtained in this study aligns broadly with published records from adjacent coastal

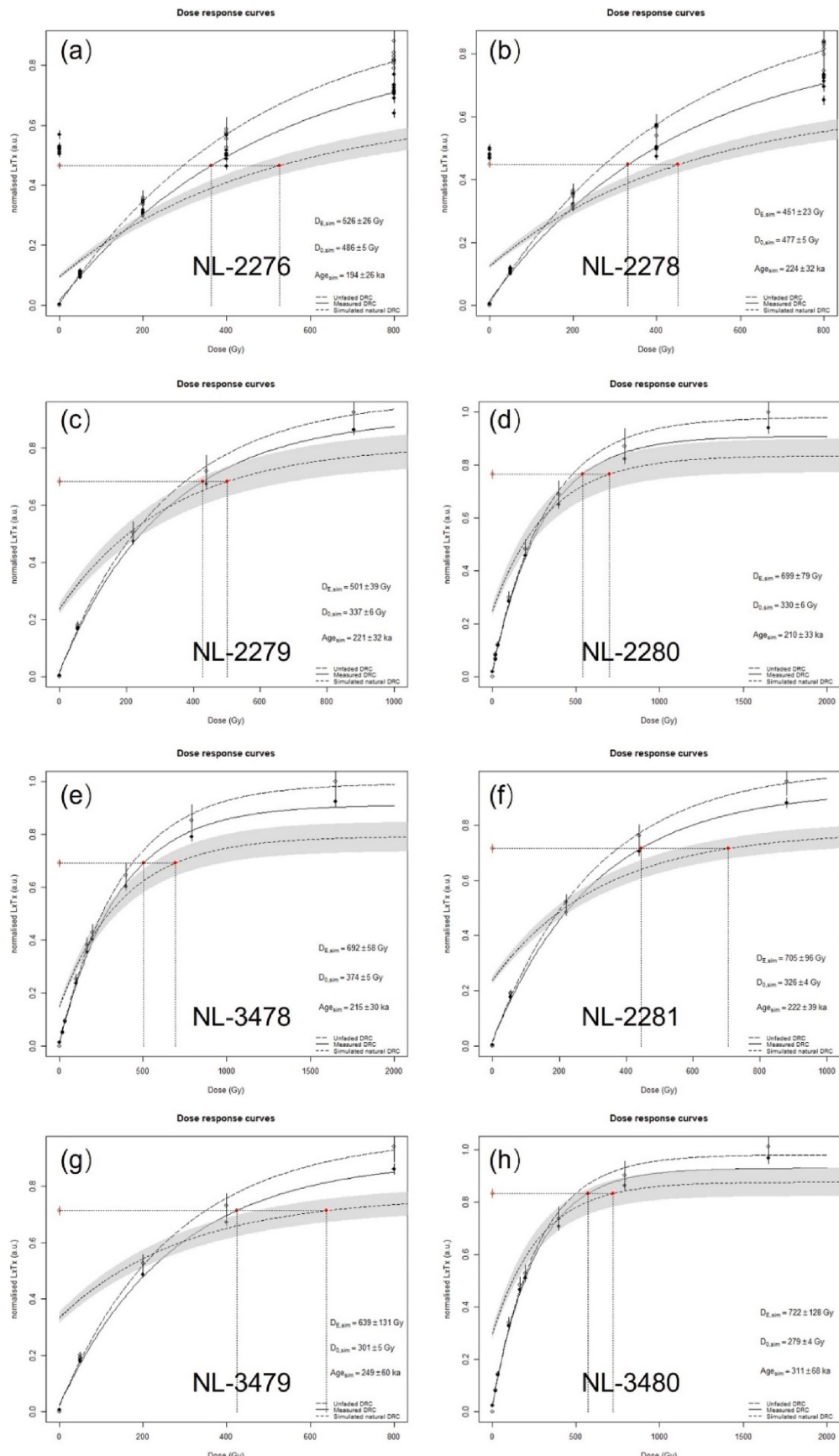


Fig. 11. (a–h) Luminescence age fading correction results for PM and KFS grains pIRIR₂₂₅ signals.

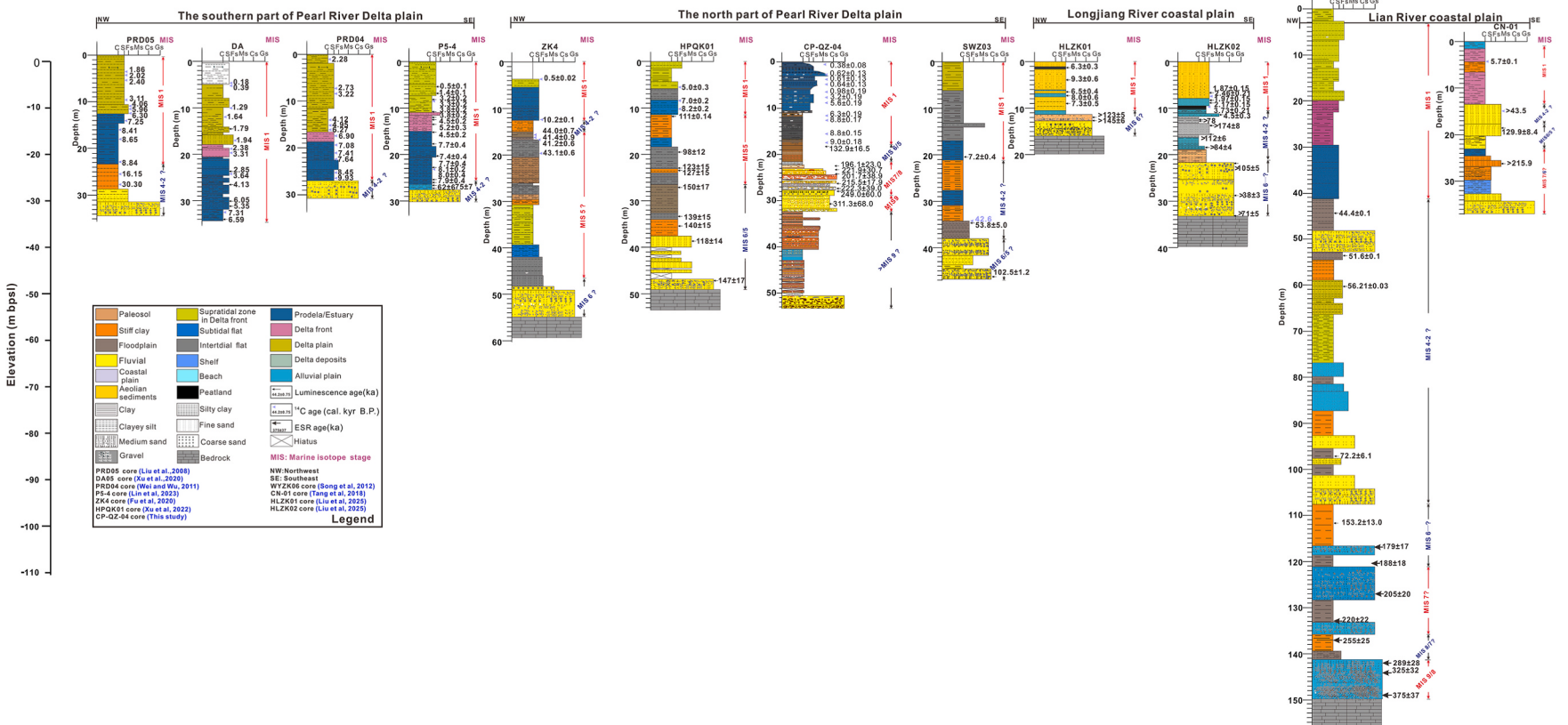


Fig. 12. Chronostratigraphic correlation of core CP-QZ04 with regional sedimentary records, including cores from the southern part of the Pearl River Delta, the northern part of Pearl River Delta, Longjiang River coastal plain, and Lian River coastal plain.

to neritic environments (Figs. 1 and 12), including cores data from the Lianjiang River coastal basin (Song et al., 2012; Tang et al., 2018), the Chaoshan plain neritic region (Zhong et al., 2023), the Longjiang Plain in northern coastal south China Sea (Liu et al., 2025), and the Pearl River Delta inland plain (Xu et al., 2020; Xu et al., 2022; Lin et al., 2022; Lin et al., 2023).

In short, these multi-faceted agreements significantly strengthen the confidence in the robustness of the new chronological framework of core CP-QZ04 in the present Pearl River Delta estuary.

5.3. The depositional evolution of the Pearl River Delta estuary region in response to global climate and sea-level change

By combining Bayesian age-depth model with sedimentological analysis of core CP-QZ04, including lithological characteristics and grain size distributions (Figs. 2–4), this study reconstructed the first depositional history spanning approximately ~311 ka for the Pearl River Delta stratigraphy in its present estuary region. The results demonstrate that the estuary's depositional evolution has undergone several distinct stages of sedimentary stacking since the mid-to-late Pleistocene, primarily driven by global climate and sea-level changes (Figs. 13 and 14). These evolutionary stages can be summarized as follows.

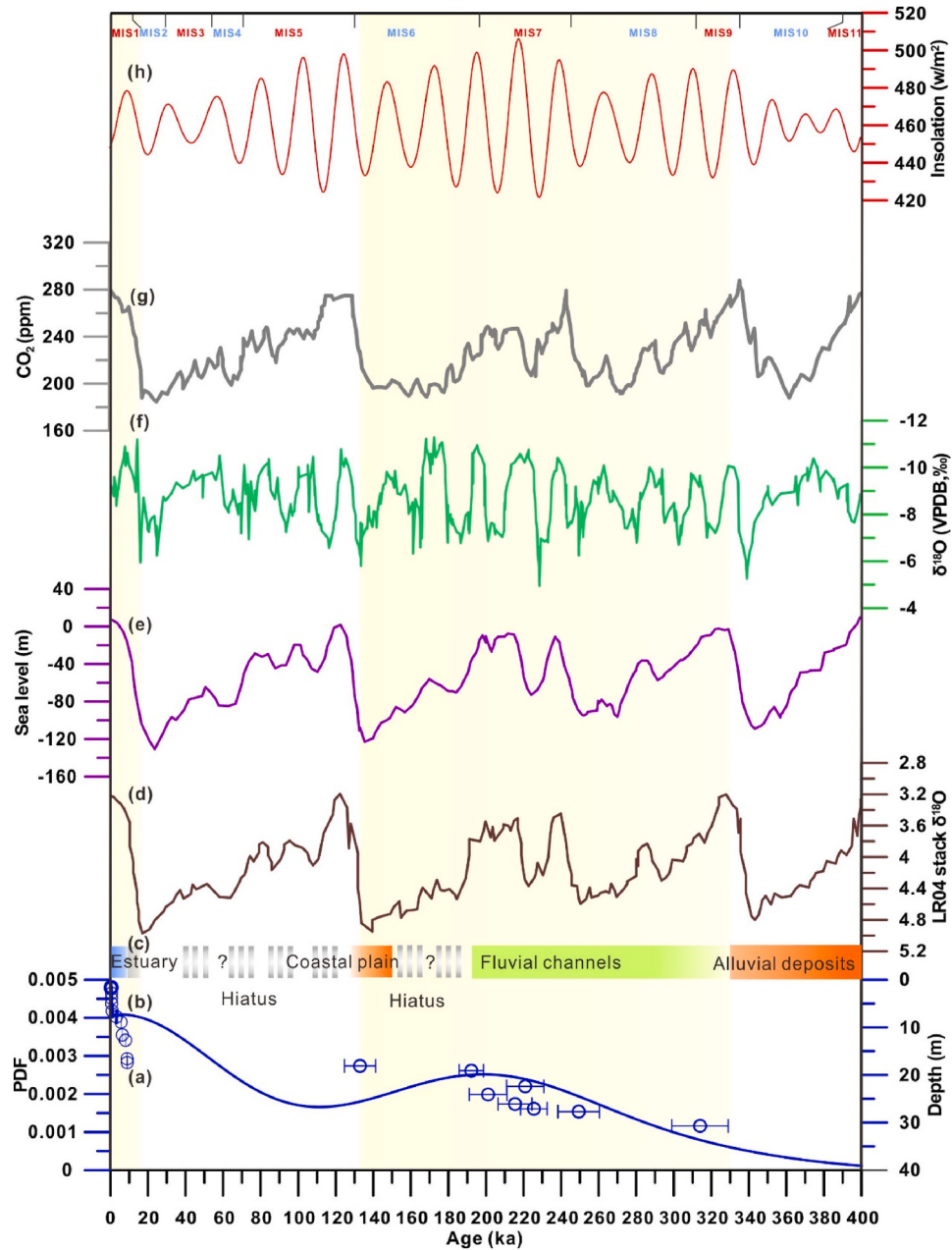


Fig. 13. Correlation and comparison of the newly reconstructed chronostratigraphy record for the Pearl River Delta estuary with global climate and sea-level changes. (a) Age-depth relationship of core CP-QZ04 (this study); (b) Probability density function (PDF) of the composite ages of core CP-QZ04 (this study); (c) Temporal variation of the sedimentary sequence of core CP-QZ04 (this study); (d) Global glacial-interglacial climate record based on LR04 benthic stack $\delta^{18}\text{O}$ data (Lisiecki and Raymo, 2005); (e) Global sea-level changes during glacial-interglacial cycles (Grant et al., 2014); (f) Asian monsoon variation recorded by Cave speleothem $\delta^{18}\text{O}$ data (Cheng et al., 2016); (g) Atmosphere CO_2 concentration change in glacial-interglacial timescales (Bereiter et al., 2015); (h) 25°N summer insolation at variation in glacial-interglacial timescales (Berger, 1978).

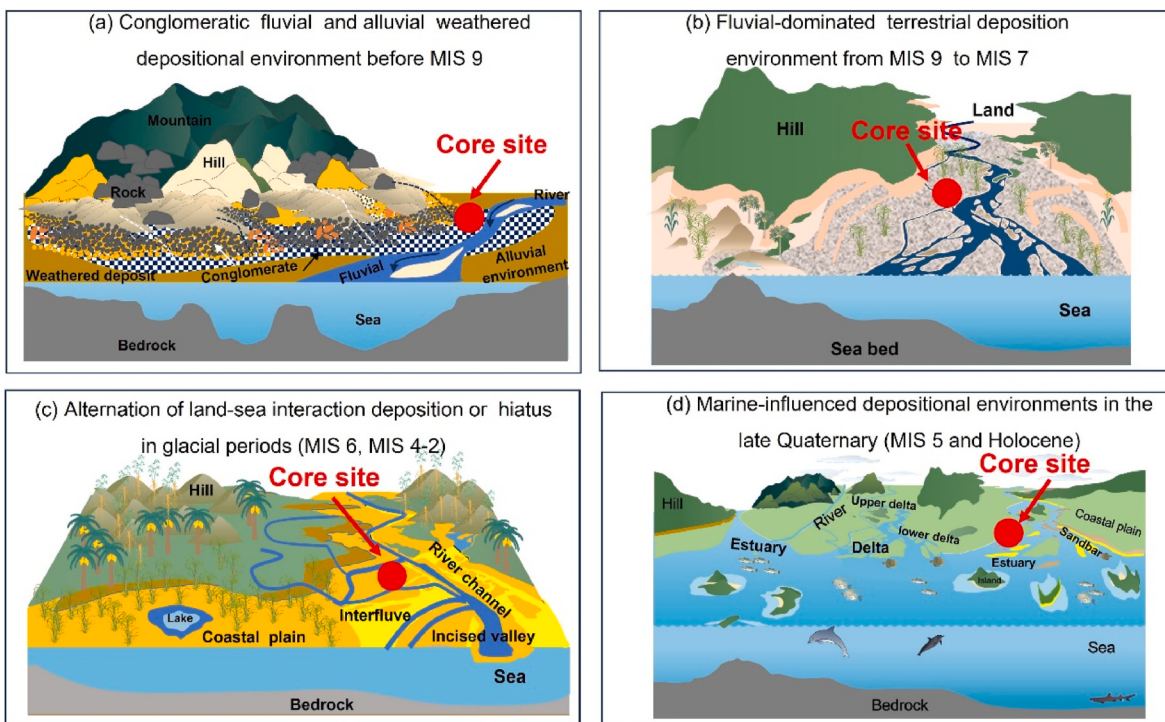


Fig. 14. Sketch map illustrating variations in depositional environments in response to global climate-induced sea-level changes since the late Quaternary. (a) Conglomeratic fluvial and alluvial weathered depositional environments before MIS 9; (b) Fluvial-dominated terrestrial depositional environments from MIS 9 to MIS 7; (c) Alternation phases of terrestrial-marine interaction and/or depositional hiatus (e.g., MIS6, MIS4-2) during glacial periods; (d) Marine-influenced depositional environments in the late Quaternary (MIS 5 and Holocene).

5.3.1. Conglomeratic fluvial and alluvial weathered deposits formed before MIS 9

The lower sedimentary stratigraphy (53–30.7 m) of core CP-QZ04 comprise conglomeratic fluvial deposits (Fig. 3n) and alluvial weathered sediments (Fig. 3l and m). These features indicate a terrestrially dominated depositional environment in the present Pearl River Delta estuary region, likely associated with climate and sea-level fluctuation prior to MIS 9 (>311 ka, Fig. 14a). This setting is inferred to correspond to MIS 10 or an earlier period, when global sea levels declined to a lowstand (Fig. 13e; Grant et al., 2014; Rohling et al., 2014). Coupled with global cooling, driven by reduced insolation and atmospheric CO₂ (Fig. 13g; Bereiter et al., 2015) and a weakened Asian monsoon (Figs. 13e and 14a; Cheng et al., 2016), these factors promoted terrestrial dominance in the region. Nevertheless, due to limited robust age constraints, previous studies have largely overlooked linkages between the Pearl River Delta sedimentary records and climate change during this period, focusing instead on regional stratigraphic analysis (Chen, 1987; Huang et al., 2021). However, high-resolution studies of the Pearl River Mouth Basin, suggest that shelf-margin prism architecture and stratal stacking patterns preserve signatures of glacio-eustatic cycles and paleoclimate variability across different geological timescales (He et al., 2017; Liu et al., 2022a). For instance, intensified climate variability and strengthened monsoons during and after the mid-Pleistocene transition may have enhanced sediment supply, facilitating the development of shelf-to-shelf-edge delta systems (Liu et al., 2022a). Such cases provide potential analogs for our reconstructed pre-MIS 9 depositional regime.

5.3.2. Fluvial-dominated terrestrial deposition from MIS 9 to MIS 7

The probability density function (PDF) and age clusters (Fig. 13a and b) of the sedimentary sequence strongly indicate that depositional environments in the Pearl River Delta estuary region during MIS 9 to MIS 7 were dominated by fluvial-terrestrial processes (Fig. 3h–k, 13c and 14b). Notably, the stratigraphical ages primarily cluster within MIS 7, with only one exception in MIS 9. This pattern likely reflects sedimentary

responses to glacio-eustatic cycles and paleoclimate variability.

Although previous studies have pointed out distinct differences in the distribution of the Pearl River Delta fluvial gravels before and after the Late Pleistocene's first transgression, attributed paleo-drainage reorganization caused by fault activities (Yao et al., 2013), our findings align with broader regional trends (Fig. 12). Both the depositional patterns identified in this study and long-term geological records from Pearl River Delta mouth basin (He et al., 2017; Liu et al., 2022a) correlate with interglacial conditions during MIS 9 and MIS 7, characterized by high sea levels, warmer global climate, and enhanced Asian monsoon intensity (Fig. 13; Grant et al., 2014; Rohling et al., 2014; Cheng et al., 2016). These observations suggest that the Pearl River Delta estuary's sedimentary sequences were primarily controlled by Milankovitch-paced glacio-eustatic and climate cycles during the mid-Pleistocene, albeit modulated by local sediment supply and tectonic influences (Fig. 13; He et al., 2017; Liu et al., 2022a).

Moreover, our new chronostratigraphic evidence confirmed that the first transgressive deposition in the late Quaternary Pearl River Delta stratigraphy postdates MIS 7. These findings provide robust chronological constraints that validate previous hypothesis derived from stratigraphic analyses and stacking pattern interpretations (Zong et al., 2016; Fu et al., 2020b; Huang et al., 2021; Lu et al., 2023; Zheng et al., 2023). These earlier studies, based on late Quaternary stratigraphy, had inferred only two marine transgression events, with the timing of the first transgressive deposition occurring during MIS5 rather than MIS 7 or earlier.

5.3.3. Alternating terrestrial-marine deposition and hiatuses since MIS 6

The chronostratigraphic framework of this study (Fig. 2) reveals that the depositional environments in the present Pearl River Delta estuary region evolved from a coastal plain during MIS 6 (Fig. 3f and g) to the Holocene muddy tidal flat and prodelta settings (Figs. 3a–e and 14). Notably, a significant depositional hiatus occurred from the last interglacial (MIS 5) through the last glacial period (MIS 4–2).

During MIS 6, the present Pearl River Delta estuary region was characterized by a coastal plain environment (Fig. 14c). However, the study core site exhibits a depositional hiatus during MIS 4–2. Although global climate and sea level shifted from interglacial to glacial conditions in both MIS 6 and MIS 4–2 (Fig. 14c), as evidenced by proxy indicator in Fig. 13d–h, the deposition records and preservation between these periods differ significantly. These divergent sediment stacking and preservation patterns may reflect variations in paleo-topography influenced by tectonic subsidence processes (Yao et al., 2013; Yu et al., 2016; Zong et al., 2016; Su et al., 2020; Huang et al., 2021).

Given relatively elevated paleo-topography, a terrestrial-dominated coastal plain developed and was preserved during MIS 6. With persistent tectonic subsidence, the present Pearl River Delta estuary region had subsided to near-modern sea level by MIS 5 (Yim et al., 1990, 1999; Zong et al., 2016). Notably, the chronostratigraphic record in this study reveals an absent of MIS 5 successions. When comparing the studied core site (estuary) with previous findings from the Pearl River Delta inland plain (Zong et al., 2009b; Fu et al., 2020b; Huang et al., 2021; Lu et al., 2023), the lack of MIS 5 transgressive deposits in its modern estuary region may reflect a depocenter shift driven by global climate change induced sea-level fluctuations during the MIS 5, followed by erosion during subsequent sea-level fall during the last glacial period.

From MIS 4 to MIS 2, sedimentary records as suggested by regional stratigraphic correlations of regional cores (Fig. 12) exhibit widespread erosional features and depositional hiatuses (Fig. 14c), primarily controlled by eustatic sea-level decline and intensified climatic oscillations. Interestingly, sedimentary records from adjacent coastal zones in southern China exhibit comparable depositional hiatuses to those observed in this study (Fig. 12). For instance, Lin et al. (2023, 2024) documented two distinct sedimentary sequences in the Pearl River Delta that display pronounced depositional gaps during ~70–8 ka and ~35–5 ka. Similarly, borehole cores from the Longjiang River coastal plain reveal significant hiatuses between $>123 \pm 8$ ka and 7.6 ka, and between $>72 \pm 4$ ka and ~5.1 ka (Liu et al., 2025, Fig. 12). These consistent sedimentary gaps across regions unequivocally reflect terrestrial dominance during periods of falling sea levels MIS 4–2 (Fig. 13).

Regarding the Holocene sedimentary evolution of the Pearl River Delta estuary, the reconstructed stratigraphy reveals a transition from muddy tidal flat deposition (9–8 ka) to prodelta sedimentation (after 5 ka) (Figs. 2 and 3a–e). The chronostratigraphic framework established in this study aligns with the well-documented Holocene sedimentary history of the Pearl River Delta (Zong, 2004; Zong et al., 2009a, 2012; Xiong et al., 2018a, 2018b; Xu et al., 2020; Lin et al., 2022a; Chen et al., 2023). As shown in Fig. 12, these regionally correlated sedimentary successions document a progressive marine transgression during the early Holocene, driven by postglacial sea-level rise (Figs. 13 and 14d), followed by a transition to regressive conditions in the middle-to-late Holocene as decreased rates of sea-level rise. However, in contrast to the Late Pleistocene sedimentary processes described above, the Holocene evolution of the Pearl River Delta has been governed by a more complex interplay of three key drivers: 1) sea-level fluctuations, 2) monsoon climate dynamics, and 3) anthropogenic influences. This evolutionary pattern is well exemplified by Zong et al. (2009a), who reconstructed the 9000-year development history of the delta and investigated land-sea interactions in this large deltaic complex under the influence of Asian monsoon climate. Their study revealed that deltaic sequences formation began during a period of rapid sea-level rise between 9000 and 7000 cal yr BP. When the sea-level rise markedly decreased around 7000 cal yr BP, the sedimentation regime switched from transgressive to regressive. During the initial phase, both the delta plains progradation near the apex and delta front aggradation in the central and lower basin occurred rapidly due to strong monsoonal-driven runoff. The progradation rate gradually slowed down in the range of 6800–2000 cal yr BP as monsoonal intensity weakened. Rapid shoreline migrations seaward during the last 2000 years were

primarily attributed to significantly intensified human activities, particularly sediment trapping in encircled tidal flats along delta plain margins. These findings have been corroborated by multiple lines of evidence, including sedimentary and microfossil diatom analyses of core sediments (Zong et al., 2012), sea-level index point data (Xiong et al., 2018a), and paleo-shoreline reconstruction (Xiong et al., 2020b).

6. Conclusion

This study establishes a robust chronostratigraphic framework spanning approximately 311 ka to constrain the late Quaternary sedimentary evolution of the modern Pearl River Delta estuary. Our approach integrates sedimentological analyses of a 53-m-long drill core with radiocarbon (^{14}C) dating and multi-method luminescence dating techniques, including quartz OSL, PM grains, and SA/SG KFS pIRIR₂₂₅. The resulting chronostratigraphy reveals a complex depositional successions during the Late Quaternary, characterized by conglomeratic fluvial and alluvial weathered deposits before MIS 9. From MIS 9 to MIS 7, fluvial-dominated terrestrial deposition prevailed, followed by the development of coastal plain environments during MIS 6. These successions are ultimately capped by the Holocene muddy tidal flat and prodela deposits. Notably, significant depositional hiatuses are identified during MIS 5 and MIS 4–2, which may be attributed to subaerial exposure and erosion associated with sea-level fluctuations or shifts in sediment depocenters. Overall, these observed patterns of terrestrial-marine interaction are primarily governed by global climate and sea-level fluctuations linked to glacial-interglacial cycles. These climate variations facilitated increased terrestrial sediment input during warm interglacial periods, while marine influence intensified during relative sea-level highstands, albeit modulated by local sediment supply and tectonic conditions. These identified phases of deposition and erosion exhibit strong correlations with regional coastal records, highlighting the dominant role of global climatic and eustatic controls in shaping the evolution of delta-estuary systems.

This study significantly advances our understanding of coastal systems responses to Quaternary environmental change, while demonstrating the efficacy of combining multi-method luminescence dating in reconstructing complex depositional histories. The Pearl River Delta's sedimentary archive not only provides a stratigraphic benchmark for regional paleoenvironmental reconstructions but also offers critical insights into future coastal system resilience under accelerating climate-driven sea-level rise scenarios.

Credit authorship contribution statement

Lei Gao: Conceptualization, Methodology, Data curation, Software, Visualization, Writing – original draft, Writing – review & editing. **Hao Long:** Funding acquisition, Software, Data curation, Formal analysis, Writing-reviewing & editing. **Jingran Zhang:** Software, Visualization, Data curation, Writing-reviewing & editing. **Xiaoling Huang:** Methodology, Data curation, Formal analysis. **Zhigang Zhang:** Software, Data curation. **Aimin Zhang:** Methodology, Formal analysis. **Leilei Yuan:** Investigation, Formal analysis, Visualization. **Xiaohua Zhou:** Funding acquisition, Writing-reviewing & editing. **Ren Jiang:** Funding acquisition, Writing-reviewing & editing.

Declaration of competing interest

The authors declare that they have no competing financial interest or personal relationships that could have appeared to influence the work reported in this paper.

Acknowledgement

This research was supported by the following funding sources: Geological Survey in Key Economic Zones and New Urban Areas (Grant

No. DD20240025), National Natural Science Foundation of China (Grant Nos. 42471008 and 41807417), Regional Geological Survey of the Yangtze River Delta Economic Zone (Grant No. DD20230201), Jiangsu Province Special Innovation Fund for Carbon Peak and Carbon Neutrality-Major Scientific and Technological Demonstration Project (Grant No. BE2022859), and NIGLAS Science and Technology Planning Project (Grant No. NIGLAS2022GS01). We sincerely thank Lili Liu for her assistance in the process of sediment samples preparation for luminescence measurements. We also deeply appreciate the constructive comments and suggestions provided by two anonymous reviewers, which significantly improved the quality of this work.

Appendix A. Supplementary data

Supplementary data to this article can be found online at <https://doi.org/10.1016/j.quascirev.2025.109609>.

Data availability

All data and/or code is contained within the submission.

References

- Adamiec, G., Aitken, M.J., 1998. Dose-rate conversion factors: update. *Ancient TL* 16, 37–50.
- Anthony, E., Svitiski, J., Zăinescu, F., Nicholls, R.J., Cohen, K.M., Marriner, N., Saito, Y., Day, J., Minderhoud, P.S.J., Amorosi, A., Chen, Z., Morhange, C., Tamura, T., Vespremeau-Stroe, A., Besset, M., Sabatier, F., Kaniewski, D., Maselli, V., 2024. Delta sustainability from the Holocene to the anthropocene and envisioning the future. *Nat. Sustain.* 7, 1235–1246.
- Atiken, M.J., 1998. An Introduction to Optical Dating. Oxford University Press.
- Auclair, M., Lamotte, M., Huot, S., 2003. Measurement of anomalous fading for feldspar IRSL using SAR. *Radiat. Meas.* 37, 487–492.
- Balescu, S., Lamotte, M., 1994. Comparison of TL and IRSL age estimates of feldspar coarse grains from waterlain sediments. *Quat. Sci. Rev.* 13, 437–444.
- Bell, W., 1979. Alpha dose attenuation in quartz grains for thermoluminescence dating. *Ancient TL* 12, 8.
- Bereiter, B., Eggleston, S., Schmitt, J., Nehrbass-Ahles, C., Stocker, T.F., Fischer, H., Kipfstuhl, S., Chappellaz, J., 2015. Revision of the EPICA dome C CO₂ record from 800 to 600 kyr before present. *Geophys. Res. Lett.* 42, 542–549.
- Berger, A., 1978. Long-term variations of daily insolation and quaternary climatic changes. *J. Atmos. Sci.* 35, 2362–2367.
- Bianchi, T.S., Allison, M.A., 2009. Large-river delta-front estuaries as natural “recorders” of global environmental change. *Proc. Natl. Acad. Sci. U. S. A.* 106, 8085–8092.
- Buylaert, J.P., Jain, M., Murray, A.S., Thomsen, K.J., Thiel, C., Sohbat, R., 2012. A robust feldspar luminescence dating method for middle and late Pleistocene sediments. *Boreas* 41, 435–451.
- Buylaert, J.P., Murray, A.S., Thomsen, K.J., Jain, M., 2009. Testing the potential of an elevated temperature IRSL signal from K-feldspar. *Radiat. Meas.* 44, 560–565.
- Chan, F.K.S., Paszkowski, A., Wang, Z., Lu, X., Mitchell, G., Tran, D.D., Warner, J., Li, J., Chen, Y.D., Li, N., Pal, I., Griffiths, J., Chen, J., Chen, W.-Q., Zhu, Y.-G., 2024. Building resilience in Asian mega-deltas. *Nat. Rev. Earth Environ.*
- Chen, H., Wang, J., Khan, N.S., Waxi, L., Wu, J., Zhai, Y., Zhang, Y., Horton, B.P., 2019. Early and late Holocene paleoenvironmental reconstruction of the pearl river Estuary, South China Sea using foraminiferal assemblages and stable carbon isotopes. *Estuar. Coast Shelf Sci.* 222, 112–125.
- Chen, P., 1987. Understanding of the Quaternary stratigraphic division in the pearl river Delta. *Pearl River Journal* 6, 16–24 (In Chinese).
- Chen, Y., Deng, B., Saito, Y., Wang, Z., Yang, X., Wu, J., 2023. Pearl river sediment dispersal over its associated delta-estuary-shelf system during the Holocene. *Sedimentology* 70, 2331–2354.
- Cheng, H., Edwards, R.L., Sinha, A., Spotil, C., Yi, L., Chen, S., Kelly, M., Kathayat, G., Wang, X., Li, X., Kong, X., Wang, Y., Ning, Y., Zhang, H., 2016. The Asian monsoon over the past 640,000 years and ice age terminations. *Nature* 534, 640–646.
- Duller, G.A.T., 2008. Single-grain optical dating of Quaternary sediments: why aliquot size matters in luminescence dating. *Boreas* 37, 589–612.
- Fu, S., Xiong, H., Zong, Y., Huang, G., 2020a. Reasons for the low sedimentation and slow progradation in the Pearl River Delta, southern China, during the middle Holocene. *Mar. Geol.* 423.
- Fu, S., Zong, Y., Xiong, H., Zhao, X., Zheng, Y., Wu, Y., Huang, G., Zhong, T., 2020b. New evidence for sea level change during the marine isotope stage 5 in the Pearl River Delta. *Quat. Sci.* 40, 1095–1104 (In Chinese with English abstract).
- Galbraith, R.F., Roberts, R.G., Laslett, G.M., Yoshida, H., Olley, J.M., 1999. Optical dating of single and multiple grains of quartz from jinmian rock shelter, northern Australia: part I, experimental design and statistical models. *Archaeometry* 41 (2), 339–364.
- Galbraith, R.F., Roberts, R.G., 2012. Statistical aspects of equivalent dose and error calculation and display in OSL dating: an overview and some recommendations. *Quat. Geochronol.* 11, 1–27.
- Gao, L., Long, H., Hou, Y., Feng, Y., 2022. Chronology constraints on the complex sedimentary stratigraphy of the paleo-Yangtze incised valley in China. *Quat. Sci. Rev.* 287, 1–19.
- Gao, L., Long, H., Shen, J., Yu, G., Liao, M., Yin, Y., 2017. Optical dating of Holocene tidal deposits from the southwestern coast of the south yellow sea using different grain-size quartz fractions. *J. Asian Earth Sci.* 135, 155–165.
- Gao, L., Long, H., Shen, J., Yu, G., Yin, Y., 2016. High-resolution OSL dating of a coastal sediment sequence from the south yellow sea. *Geochronometria* 43, 143–154.
- Gao, L., Long, H., Tamura, T., Hou, Y., Shen, J., 2021. A ~130 ka terrestrial-marine interaction sedimentary history of the northern Jiangsu coastal plain in China. *Mar. Geol.* 435, 106455.
- Gao, L., Long, H., Tamura, T., Ye, L., Hou, Y., Shen, J., 2020. Refined chronostratigraphy of a late Quaternary sedimentary sequence from the yangtze river delta based on K-feldspar luminescence dating. *Mar. Geol.* 427, 106271.
- Grant, K.M., Rohling, E.J., Ramsey, C.B., Cheng, H., Edwards, R.L., Florindo, F., Heslop, D., Marra, F., Roberts, A.P., Tamisiea, M.E., Williams, F., 2014. Sea-level variability over five glacial cycles. *Nat. Commun.* 5, 5076.
- Guérin, G., Mercier, N., Adamiec, G., 2011. Dose-rate conversion factors: update. *Ancient TL* 29, 5–8.
- Hajdas, I., Ascough, P., Garnett, M.H., Fallon, S.J., Pearson, C.L., Quarta, G., Spalding, K., Yamaguchi, H., Yoneda, M., 2021. Radiocarbon dating. *Nature Reviews Methods Primers* 1, 1–26.
- He, M., Zhuo, H., Chen, W., Wang, Y., Du, J., Liu, L., Wang, L., Wan, H., 2017. Sequence stratigraphy and depositional architecture of the pearl river Delta system, northern South China Sea: an interactive response to sea level, tectonics and paleoceanography. *Mar. Petrol. Geol.* 84, 76–101.
- Huang, P., Zhang, K., Yu, Z., Liang, H., Li, Z., Chen, Z., Tang, Y., Zeng, Q., 2021. Reanalysis of the stratigraphic sequence and new understanding of neotectonic movement of the pearl river Delta since the late Pleistocene south China. *J. Seismol.* 41, 10–20.
- Huang, Z., Li, P., Zhang, Z., Konghong, L., Qiao, P., 1982. Formation, Developement and Evolution of the Pearl River Delta. Guangzhou Branch of Popularization Science Press, Guangzhou.
- Huntley, D., Baril, M., 1997. The K Content of the K-feldspars Being Measured in Optical Dating or in Thermoluminescence Dating.
- Huntley, D.J., 2006. An explanation of the power-law decay of luminescence. *J. Phys.: Condensed Matter* 18, 1359–1365.
- Huntley, D.J., Lamotte, M., 2001. Ubiquity of anomalous fading in K-feldspars and the measurement and correction for it in optical dating. *Can. J. Earth Sci.* 38, 1093–1106.
- Jacobs, Z., 2008. Luminescence chronologies for coastal and marine sediments. *Boreas* 37, 508–535.
- Kars, R.H., Wallinga, J., Cohen, K.M., 2008. A new approach towards anomalous fading correction for feldspar IRSL dating — tests on samples in field saturation. *Radiat. Meas.* 43, 786–790.
- Kars, R.H., Reimann, T., Ankjærgaard, C., Wallinga, J., 2014. Bleaching of the post-IR IRSL signal: new insights for feldspar luminescence dating. *Boreas* 43, 780–791.
- Kenzler, M., Tsukamoto, S., Meng, S., Thiel, C., Frechen, M., Hüneke, H., 2015. Luminescence dating of Weichselian interstadial sediments from the German Baltic sea coast. *Quat. Geochronol.* 30, 251–256.
- Lamotte, M., 2016. Luminescence dating of interglacial coastal depositional systems: recent developments and future avenues of research. *Quat. Sci. Rev.* 146, 1–27.
- Lancia, M., Su, H., Tian, Y., Xu, J., Andrews, C., Lerner, D.N., Zheng, C., 2020. Hydrogeology of the pearl river Delta, southern China. *J. Maps* 16, 388–395.
- Li, B., Li, S.-H., 2012. A reply to the comments by Thomsen et al. on “Luminescence dating of K-feldspar from sediments: a protocol without anomalous fading correction”. *Quat. Geochronol.* 8, 49–51.
- Li, B., Jacobs, Z., Roberts, R.G., 2023. A Bayesian hierarchical age model for optical dating of single grains of quartz. *Quat. Geochronol.* 77.
- Li, B., Jacobs, Z., Roberts, R.G., Li, S.H., 2014. Review and assessment of the potential of post-IR IRSL dating methods to circumvent the problem of anomalous fading in feldspar luminescence. *Geochronometria* 41, 178–201.
- Li, B., Jacobs, Z., Roberts, R.G., Li, S.-H., 2018. Single-grain dating of potassium-rich feldspar grains: towards a global standardised growth curve for the post-IR IRSL signal. *Quat. Geochronol.* 45, 23–36.
- Li, B., Roberts, R.G., Jacobs, Z., Li, S.-H., 2015a. Potential of establishing a ‘global standardised growth curve’ (gSGC) for optical dating of quartz from sediments. *Quat. Geochronol.* 27, 94–104.
- Li, B., Roberts, R.G., Jacobs, Z., Li, S.-H., Guo, Y.-J., 2015b. Construction of a ‘global standardised growth curve’ (gSGC) for infrared stimulated luminescence dating of K-feldspar. *Quat. Geochronol.* 27, 119–130.
- Li, Y., Tsukamoto, S., Shang, Z., Tamura, T., Wang, H., Frechen, M., 2019. Constraining the transgression history in the bohai Coast China since the middle Pleistocene by luminescence dating. *Mar. Geol.* 416, 105980.
- Liang, P., Forman, S.L., 2019. LDAC: an Excel-based program for luminescence equivalent dose and burial age calculations. *Ancient TL* 37, 22–40.
- Lin, P., Song, Y., Zhan, W., Tian, R., Wang, Z., Xu, X., Luo, L., Abbas, M., Lai, Z., 2022a. Holocene sedimentary of the pearl river Delta in south China: OSL and radiocarbon dating of cores from zhuhai. *Front. Mar. Sci.* 9, 1031456. <https://doi.org/10.3389/fmars.2022.1031456>.
- Lin, P., Song, Y., Zhan, W., Tian, R., Wang, Z., Xu, X., Luo, L., Abbas, M., Lai, Z., 2022. Holocene sedimentary of the Pearl River Delta in South China: OSL and radiocarbon dating of cores from Zhuhai. *Front. Mar. Sci.* 9, 1031456. <https://doi.org/10.3389/fmars.2022.1031456>.

- Lin, P., Song, Y., Zhan, W., Tian, R., Wang, Z., Xu, X., Luo, L., Abbas, M., Lai, Z., 2023. Late Pleistocene to Holocene sedimentary history in the pearl river Delta revealed by OSL and radiocarbon dating. *Catena* 224.
- Lin, P., Xu, X., Yan, C., Luo, L., Abbas, M., Lai, Z., 2022b. Holocene sedimentary of the pearl river delta in south China: OSL and radiocarbon dating of cores from zhuhai. *Front. Mar. Sci.* 8, 1–15.
- Lisiecki, L.E., Raymo, M.E., 2005. A Pliocene-Pleistocene stack of 57 globally distributed benthic δ₁₈O records. *Paleoceanogr.* 20, 1–17.
- Liu, H., Lin, C., Zhang, Z., Zhang, B., Tian, H., Zhang, M., Jiang, J., 2022a. Shelf-margin architecture and deposition variability across the mid-pleistocene climate transition, northeastern South China Sea. *Mar. Geol.* 443, 106690.
- Liu, R., Nian, X., Zhang, W., Qiu, F., Wang, Z., Lin, Q., Shu, J., Liu, N., 2022b. Luminescence dating of the late Quaternary sediments in Hangzhou Bay, China. *Quat. Geochronol.* 70.
- Liu, Y., Wu, Z., Long, G., Feng, X., Lai, P., Fang, Z., Wu, W., Xu, J., Xu, G., Tu, H., Li, H., Wang, W., Lai, Z., 2025. Response to sea-level change in a non-deltaic coastal plain: insights from cores chronologies. *Geomorphology* 476.
- Liu, C.L., TFursich, F., Dong, Y.X., Che, X.G., Chen, L., Zhuang, C., 2008. High resolution ostracod records of borehole PRD05 and the late Quaternary palaeoenvironment in the Pearl River Delta. *J. Palaeogeogr.* 10, 313–322 (In Chinese with English abstract).
- Long, H., Zhang, J., Huang, X., Zhang, A., Yang, N., He, M., Yang, L., 2024. Single-grain K-feldspar luminescence dating of the late Quaternary rapid decline in the largest Lake over the Tibetan Plateau. *Quaternary Geochronology* 81, 101503.
- Long, H., Zhang, J., Zhang, S., Hou, Y., Wu, Y., Yang, N., Zhang, C., Cheng, L., Zhao, Z., Cheng, J., Shen, J., 2025. The westerlies-monsoon interaction shaped asymmetric lake expansions over the Tibetan Plateau in warming periods. *Sci. Bull.* <https://dx.doi.org/10.1016/j.scib.2025.07.023>.
- Lowik, S.E., Trauerstein, M., Preusser, F., 2012. Testing the application of post IRIRSL dating to fine grain waterlain sediments. *Quaternary Geochronology* 8, 33–40.
- Lu, H., Jiang, S., Huang, K., Cheng, C., Tang, Y., Li, H., Huang, P., Huang, K., 2023. Sedimentary sequences in response to marine transgression during the late Quaternary, pearl river delta. *Mar. Geol. Quat. Geol.* 43, 18–30.
- Mahan, S.A., Rittenour, T.M., Nelson, M.S., Attaee, N., Brown, N., DeWitt, R., Durcan, J., Evans, M., Feathers, J., Frouin, M., Guérin, G., Heydari, M., Huot, S., Jain, M., Keen-Zebert, A., Li, B., López, G.I., Neudorf, C., Porat, N., Rodrigues, K., Sawakuchi, A.O., Spencer, J.Q.G., Thomsen, K., 2022. Guide for interpreting and reporting luminescence dating results. *GSA Bulletin*.
- Mauz, B., Packman, S., Lang, A., 2006. The alpha effectiveness in silt-sized quartz-New data obtained by single and multiple aliquot protocols. *Ancient TL* 24, 47–52.
- Mejdahl, V., 1979. Thermoluminescence dating: beta-dose attenuation in quartz grains. *Archaeometry* 21, 61–72.
- Murray, A., Arnold, L.J., Buylaert, J.-P., Guérin, G., Qin, J., Singhvi, A.K., Smedley, R., Thomsen, K.J., 2021. Optically stimulated luminescence dating using quartz. *Nat. Rev. Methods Primers* 1, 1–72.
- Murray, A.S., Wintle, A.G., 2000. Luminescence dating of quartz using an improved single aliquot regenerative dose protocol. *Radiat. Meas.* 32, 57–73.
- Nienhuis, J.H., Ashton, A.D., Edmonds, D.A., Hoitink, A.J.F., Kettner, A.J., Rowland, J.C., Tornqvist, T.E., 2020. Global-scale human impact on delta morphology has led to net land area gain. *Nature* 577, 514–518.
- Peng, J., Li, B., 2017. Single-aliquot regenerative-dose (SAR) and standardised growth curve (SGC) equivalent dose determination in a batch model using the R package ‘numOSL’. *Ancient TL* 35, 32–53.
- Prescott, J.R., Hutton, J.T., 1994. Cosmic ray contributions to dose rates for luminescence and ESR dating: large depths and long-term time variations. *Radiat. Meas.* 23, 497–500.
- Qin, J., Chen, J., Li, Y., Zhou, L., 2018. Initial sensitivity change of K-feldspar pIRIR signals due to uncompensated decrease in electron trapping probability: evidence from radiofluorescence measurements. *Radiat. Meas.* 120, 131–136.
- Rees-Jones, J., 1995. Optical dating of young sediments using fine-grain quartz. *Ancient TL* 13, 9–14.
- Reimann, T., Thomsen, K.J., Jain, M., Murray, A.S., Frechen, M., 2012. Single-grain dating of young sediments using the pIRIR signal from feldspar. *Quat. Geochronol.* 11, 28–41.
- Riedesel, S., Brill, D., Roberts, H.M., Duller, G.A.T., Garrett, E., Zander, A.M., King, G.E., Tamura, T., Burow, C., Cunningham, A., Seeliger, M., De Batist, M., Heyvaert, V.M. A., Fujiwara, O., Brückner, H., 2018. Single-grain feldspar luminescence chronology of historical extreme wave event deposits recorded in a coastal lowland, Pacific coast of central Japan. *Quat. Geochronol.* 45, 37–49.
- Rohling, E.J., Foster, G.L., Grant, K.M., Marino, G., Roberts, A.P., Tamisiea, M.E., Williams, F., 2014. Sea-level and deep-sea-temperature variability over the past 5.3 million years. *Nature* 508, 477–482.
- Secretariat of Greater Bay Area Science Forum, 2024. Creating a new source of ideas by promoting intellectual exchange, talent attraction, policy consultation and technological innovation-Retrospect and prospect of Greater Bay Area Science Forum. *Bull. Chin. Acad. Sci* 39 (9), 1639–1646. <https://dx.doi.org/10.16418/j.issn.1000-3045.20240907003> (in Chinese).
- Sheng, C., Jiao, J., Zhang, J., Yao, Y., Luo, X., Yu, S., Ni, Y., Wang, S., Mao, R., Yang, T., Zhan, L., 2024. Evolution of groundwater system in the pearl river Delta and its adjacent shelf since the late Pleistocene. *Sci. Adv.* 10, 1–10.
- Smedley, R.K., 2018. Telling the time with dust, sand and rocks. *Elements: An International Magazine of Mineralogy, Geochemistry, and Petrology* 14 (1), 9–14.
- Smedley, R.K., Buylaert, J.P., Újvári, G., 2019. Comparing the accuracy and precision of luminescence ages for partially-bleached sediments using single grains of K-feldspar and quartz. *Quat. Geochronol.* 53, 101007.
- Song, Y.S., Chen, W., Pan, H., Zhang, Z., He, Z., Chen, X., Zeng, Q., Zeng, Y., Zhang, J., 2012. Geological age of Quaternary series in lianjiang plain. *J. Jilin Univ. (Eng. Technol. Ed.)* 42, 154–162.
- Strong, D., Flecker, R., Valdes, P.J., Wilkinson, I.P., Rees, J.G., Michaelides, K., Zong, Y., Lloyd, J.M., Yu, F.L., Pancost, R.D., 2013. A new regional, mid-holocene palaeoprecipitation signal of the Asian summer monsoon. *Quat. Sci. Rev.* 78, 65–76.
- Su, M., Lin, Z., Wang, C., Kuang, Z., Liang, J., Chen, H., Liu, S., Zhang, B., Luo, K., Huang, S., Wu, Q., 2020. Geomorphologic and infilling characteristics of the slope-confined submarine canyons in the pearl river mouth basin, northern South China Sea. *Mar. Geol.* 424.
- Tang, C., Zhou, D., Endler, R., Lin, J., Harff, J., 2010. Sedimentary development of the pearl river Estuary based on seismic stratigraphy. *J. Mar. Syst.* 82, S3–S16.
- Tang, Y., Chen, G., Peng, Z., Zhang, K., 2011. Late Quaternary tectonics of the pearl river Delta, SE China: evidence from xilingang. *Geodin. Acta* 24, 133–139.
- Tang, Y., Zheng, Z., Chen, C., Wang, M., Chen, B., 2018. Evolution of the lian river coastal basin in response to Quaternary marine transgressions in southeast China. *Sediment. Geol.* 366, 1–13.
- Wang, Y., Li, G., Wang, X., Yan, Z., Qin, C., Yang, J., Yang, H., Deng, Y., Pan, L., Chen, C., Zhao, W., Hou, G., 2022. Single-grain K-feldspar pIRIR dating of the shalongka archaeological site revealed the relationship between monsoon, overbank flooding, and human occupation during the Holocene on the northeastern Tibetan Plateau. *Quat. Sci. Rev.* 298, 107848.
- Wei, X., Wu, C., 2011. Holocene delta evolution and sequence stratigraphy of the pearl river Delta in south China. *Sci. China Earth Sci.* 54, 1523–1541.
- Wintle, A.G., 1973. Anomalous fading of thermoluminescence in mineral samples. *Nature* 245, 143–144.
- Xiong, H., Zong, Y., Huang, G., Fu, S., 2018a. Sedimentary responses to Holocene sea-level change in a shallow marine environment of southern China. *J. Asian Earth Sci.* 166, 95–106.
- Xiong, H., Zong, Y., Qian, P., Huang, G., Fu, S., 2018. Holocene sea-level history of the northern coast of South China Sea. *Quat. Sci. Rev.* 194, 12–26.
- Xiong, H., Zong, Y., Huang, G., Fu, S., 2020. Human drivers accelerated the advance of Pearl River Deltaic shoreline in the past 7500 years. *Quat. Sci. Rev.* 246.
- Xiong, H., Zong, Y., Qian, P., Huang, G., Fu, S., 2018b. Holocene sea-level history of the northern coast of South China Sea. *Quat. Sci. Rev.* 194, 12–26.
- Xu, X., Li, H., Tang, L., Lai, Z., Xu, G., Zhang, X., Wang, Y., 2020. Chronology of a Holocene core from the pearl river Delta in southern China. *Front. Earth Sci.* 8.
- Xu, X., Zhong, J., Huang, X., Li, H., Ding, Z., Lai, Z., 2022. Age comparison by luminescence using quartz and feldspar on core HPQK01 from the Pearl River Delta in China. *Quat. Geochronol.* 71, 101320.
- Yao, Y., Zhan, W., Liu, Z., Zhang, Z., Zhan, M., Sun, J., 2013. Neotectonics and its relations to the evolution of the pearl river Delta, Guangdong, China. *J. Coast Res.* 66, 1–11.
- Yim, W.W.-S., 1999. Radiocarbon dating and the reconstruction of late Quaternary sea-level changes in Hong Kong. *Quat. Int.* 55, 77–91.
- Yu, S., Jiao, J.J., Luo, X., Li, H., Wang, X., Zhang, X., Yao, M., Zuo, J., Liang, W., Lu, M., 2023. Evolutionary history of the groundwater system in the pearl river Delta (China) during the Holocene. *Geology* 51, 481–485.
- Yim, W.W.-S., Ivanovich, M., I, K.-F.Y., 1990. Young Age Bias of Radiocarbon Dates in Pre-Holocene Marine Deposits of Hong Kong and Implications for Pleistocene Stratigraphy. *Geo-Marine Letters* 10, 165–172.
- Yu, S., Chen, F., Huang, K., Zhou, Y., Zhu, Q., Wu, C., Zhuang, C., Cao, K., Yamin, L., Zhang, J., Zheng, Z., 2025. The vegetation response to MIS5 and MIS1 as revealed by pollen data from the pearl river estuary, China. *Palaeogeogr. Palaeoclimatol. Palaeoecol.* 662, 112774.
- Yu, Z., Zhang, K., Liang, H., Li, Z., 2016. Late Quaternary tectonic movements in the pearl river Delta, China, revealed from stratigraphic profiles. *Trop. Geogr.* 36, 334–342.
- Zhao, H., Zhang, S., Sheng, Y., Yang, Z., Wang, K., Chen, F., 2025. Timing of mega-lakes in the central-southern Tibetan Plateau constrained by K-feldspar single-grain pIRIR dating of paleo-shorelines. *Global Planet. Change* 254, 104989.
- Zhang, J., Tsukamoto, S., Nottebaum, V., Lehmkühl, F., Frechen, M., 2015. De plateau and its implications for post-IR IRSL dating of polyminal fine grains. *Quaternary Geochronology* 30, 147–153.
- Zhang, J.R., Guralnik, B., Tsukamoto, S., Ankjærgaard, C., Reimann, T., 2023. The bleaching limits of IRSL signals at various stimulation temperatures and their potential inference of the pre-burial light exposure duration. *Fronter in Earth Science* 10, 933131.
- Zhang, J., Li, P., Tomczak, M., Wang, Y., Gan, H., Cai, G., Xue, Q., Hou, J., Yi, N., Wang, B., 2024. Diatom record the holocene marine facies deposition history in inner bay of pearl river Estuary, south China. *Estuarine, Coastal and Shelf Science* 302, 108766.
- Zheng, S., Lin, Z., Li, C., Li, G., Zhuang, W., Li, S., Luo, J., Yang, F., Li, Y., 2023. Discussion on the late Quaternary initial sedimentary age and sedimentary evolution in the Pearl River Delta. *Mar. Geol. Quat. Geol.* 43, 145–156.
- Zhong, J., Ling, K., Yang, M., Shen, Q., Abbas, M., Lai, Z., 2022. Radiocarbon and OSL dating on cores from the chaoshan delta in the coastal South China Sea. *Front. Mar. Sci.* 9.
- Zhong, J., Liu, B., Ou, Y., Tian, R., Shan, J., Xu, Y., Wang, F., Abbas, M., Zhang, K., Lai, Z., 2023. An erosive neritic area of shantou in coastal NE South China Sea since at least MIS 5 revealed by OSL dating of cores. *Front. Earth Sci.* 11.
- Zhou, L., Wang, Y., Du, X., Bu, Jianjun, Wu, J., Lü, W., Liu, X., 2022. Sedimentary evolution and reconstruction of maximum coastline transgression during the late Quaternary at the Western margin of the pearl river Delta. *Acta Sedimentol. Sin.* 40, 119–135.

- Zhu, Q., Xing, F., Wang, Y.P., Syvitski, J., Overeem, I., Guo, J., Li, Y., Tang, J., Yu, Q., Gao, J., Gao, S., 2024. Hidden delta degradation due to fluvial sediment decline and intensified marine storms. *Sci. Adv.* 10, eadk1698.
- Zong, Y., 2004. Mid-holocene sea-level highstand along the southeast Coast of China. *Quat. Int.* 117, 55–67.
- Zong, Y., Huang, G., Switzer, A.D., Yu, F., Yim, W.W.-S., 2009a. An evolutionary model for the Holocene formation of the Pearl River Delta, China. *Holocene* 19, 130–142.
- Zong, Y., Huang, G., Xiong, H., Li, X., Sun, Y., 2016. Relationship between late Quaternary Lithostratigraphy, Sea-level change and tectonics in the pearl river Delta. *Trop. Geogr.* 36, 326–333.
- Zong, Y., Huang, K., Yu, F., Zheng, Z., Switzer, A., Huang, G., Wang, N., Tang, M., 2012. The role of sea-level rise, monsoonal discharge and the palaeo-landscape in the early Holocene evolution of the Pearl River Delta, southern China. *Quat. Sci. Rev.* 54, 77–88.
- Zong, Y., Yim, W.W.S., Yu, F., Huang, G., 2009b. Late Quaternary environmental changes in the pearl river mouth region, China. *Quat. Int.* 206, 35–45.